Journal of Nanobiotechnology

RESEARCH

Open Access

Dual stimuli-responsive prodrug co-delivery nanosystem of salicylic acid and bioavailable silicon for long-term immunity in plant

You Liang[1,2†], Yuehong Du[1†], Yuchen Song[1], Sijin Wang[1], Can Zhao[1], Zhiming Feng[1], Shimin Zuo[1], Fengping Yang[3], Ke Xu[1] and Zhongyang Huo[1*]

Abstract

Plant-induced resistance plays a crucial role in the plant defense system by activating intrinsic immune mechanisms. In this study, a novel amidase- and redox-responsive codelivery nanosystem was developed by covalently linking salicylic acid (SA) to functionalized disulfide-doped mesoporous silica nanoparticles (MSNs-ss-NH_2) for the efficient delivery of SA and bioavailable silicon concurrently. Physicochemical characterization confirmed the successful preparation of MSNs-ss-SA, demonstrating its structural integrity and glutathione and amidase responsive degradation mechanism. With a particle size of approximately 90 nm, MSNs-ss-SA could penetrate the stomata of rice leaves, facilitating the efficient intracellular transport of SA and bioavailable silicon. Biological activity assays revealed that MSNs-ss-SA exhibited superior efficacy in inducing resistance to rice sheath blight compared to conventional SA, which was primarily due to its ability to enhance physical barrier formation, strengthen antioxidant defense systems, upregulate the expression of key defense-related genes, and increase chitinase synthesis, collectively triggering both systemic acquired resistance and induced systemic resistance. Most importantly, biological safety assessments confirmed its excellent compatibility with rice plants, aquatic organisms, soil ecosystems, and human cell models. Therefore, the prodrug system of SA and bioavailable silicon shows a significant potential for sustainable agricultural plant disease management.

†You Liang and Yuehong Du contributed equally to this work.

*Correspondence:
Zhongyang Huo
huozy69@163.com

Full list of author information is available at the end of the article

Graphical Abstract

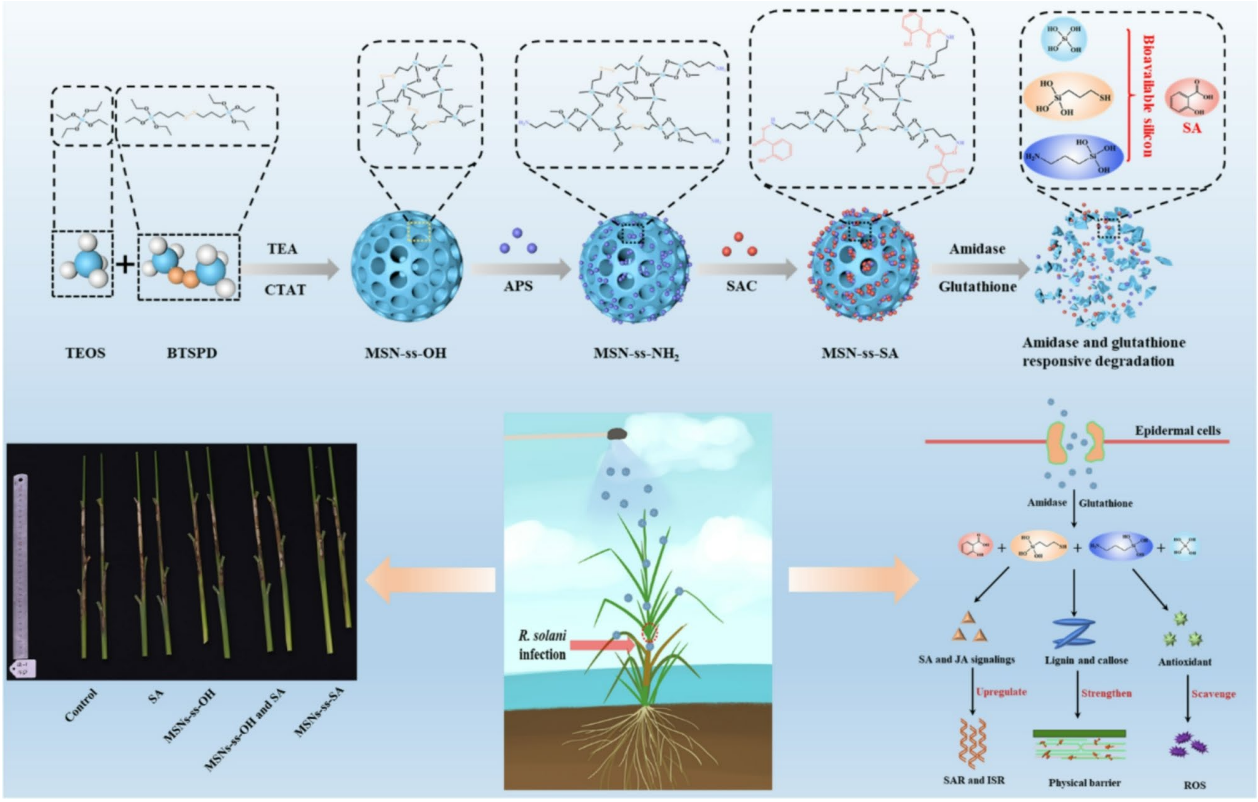

Keywords Salicylic acid, Disulfide-doped mesoporous silica nanoparticles, Bioavailable silicon, Prodrug nanosystem, Co-delivery system, Plant defense response

Introduction

Plant diseases pose a significant threat to the growth, yield, and quality of field crops, presenting considerable challenges to global agricultural productivity and food security [1]. Conventional chemical pesticides play a critical role in controlling plant diseases, thereby ensuring crop yield and food security [2, 3]. However, it is concerning that over 800,000 tons of chemical fungicides were applied globally in 2021, and more than 90% of pesticides are lost to the surrounding environment through processes such as drift, biodegradation, surface runoff, photolysis, and evaporation, leading to significant resource waste and negative environmental impacts [4–6]. Therefore, it is still a great challenge to develop eco-friendly plant immune inducers to minimize chemical fungicide usage and reduce environmental risks.

Plant immune inducers are emerging as a sustainable green strategy for plant disease management, offering an eco-friendly alternative to traditional plant disease control methods [7, 8]. Upon exposure to these inducers, plants rapidly activate their intrinsic immune defense mechanisms to induce systemic acquired resistance (SAR) throughout the entire plant, thereby enhancing its immunity resistance against pathogen invasion [9–11]. Salicylic acid (SA), a key endogenous signaling molecule in plant immunity, mediates several defense mechanisms, including the activation of SAR, the induction of disease resistance gene expression, the strengthening of physical defense barriers, the activation of antioxidant defense systems, and the promotion of chitinase synthesis, which collectively contribute to the effective defense of plants against pathogens [12]. Despite its potent immune-inducing effects on plants, high concentrations of SA can adversely affect plant growth [13–15]. Moreover, SA is rapidly metabolized within plants via glycosylation pathways, resulting in a short duration of action, which limits its effectiveness and widespread application in agricultural fields [16–19]. Therefore, developing effective strategies to reduce the toxicity of SA to plants, improving its delivery efficiency within plant tissues, and enhancing its bioavailability are of significant theoretical and practical importance for reducing the dependence on chemical fungicides and promoting sustainable crop production.

Rice, a silicon-accumulating crop, stores more than 10% silica in its stem and leaf dry weights, which is ten times greater than that of nitrogen and twenty times greater than that of phosphorus [20, 21]. Studies have demonstrated that the exogenous application of inorganic silica nanoparticles could induce disease resistance at the physiological, biochemical, and molecular levels by significantly increasing the available silicon content in rice plants [22–25]. At the physiological level, the deposition of silica in the epidermal cell walls of rice leaves and stems forms a physical barrier that hinders or delays pathogen infection [26]. Biochemically, silica stimulates rice to rapidly produce defense compounds such as phenolics, flavonoids, lignin, callose, and plant toxins, while also increasing the activity of defense enzymes such as peroxidase, phenylalanine ammonia-lyase, polyphenol oxidase, lipoxygenase, and β-1,3-glucanase [27]. At the molecular level, silica enhances the expression of defense-related genes associated with the SA, jasmonic acid (JA), and ethylene (ET) pathways, thereby enhancing the disease resistance of rice plants [28]. However, several studies have reported that larger nanoparticle sizes may reduce the conductivity efficiency within plants [29]. Additionally, high concentrations of silica nanoparticles can cause aggregation in leaf tissues, block stomata, disrupt leaf transpiration, and lead to chlorosis [30]. Therefore, it is critical to improve the utilization efficiency of silica on leaf surfaces.

Disulfide-doped mesoporous silica nanoparticles (MSNs-ss-OH) with a high specific surface area exhibit excellent degradable properties, allowing organic silicon to decompose into small fragments containing both organic and inorganic silicon molecules in a reductive environment, thus facilitating better absorption and transport within plants [31–34]. In addition, the abundant hydroxyl functional groups on the surface of MSNs-ss-OH allow for various chemical modifications, enabling loading of different types of immune inducers, which enables the controlled release of immune inducers and bioavailable silicon concurrently, addressing common issues such as uneven release and excessive toxicity often encountered in traditional pesticide delivery methods [35–39]. Therefore, MSNs-ss-OH are an ideal carrier for loading plant immune inducers, offering significant potential for agricultural applications.

Glutathione, a thiol-containing antioxidant widely present in plant cells, plays a crucial role in the degradation of disulfide bonds in pesticide delivery systems, which has been utilized for the in vivo transport of plant immune inducers [29, 40, 41]. Amidase can hydrolyze amide compounds into corresponding acids and amines, which is abundant in rice plants and is usually used to detoxify amide herbicides [42–44]. In this study, a dual stimuli-responsive prodrug nanosystem (MSNs-ss-SA) was synthesized by conjugating SA to functionalized disulfide-doped mesoporous silica nanoparticles (MSNs-ss-NH_2) via amide bonds to facilitate the efficient delivery of SA and bioavailable silicon concurrently. The synthesized MSNs-ss-SA were extensively characterized, and its biological activity was systematically evaluated using rice plants and rice sheath blight disease as target models. The study revealed the relationships between the concentrations of SA and bioavailable silicon and their respective impacts on biological activity, physical barriers, defense-related enzyme activities, and endogenous hormone contents. Additionally, the safety profile of the prodrug nanosystem, and its potential effects on rice yield and quality were also explored.

Experimental

Materials

Salicylic acid (SA, purity 98.0%), cetyltrimethylammonium p-toluenesulfonate (CTAT), bis(trimethoxysilylpropyl)disulfide (BTSPD), tetraethyl orthosilicate ester (TEOS), ammonium nitrate, and 3-Aminopropyltrimethoxysilane (APS) were purchased from Tianjin Heowns Biochemical Technology Co., Ltd. (Tianjin, China). Amidase (from *Pseudomonas aeruginosa*, with hydroxamate transferase activity ≥ 200 units/mg protein, molecular weight around 228 kDa) and glutathione were obtained from Sigma-Aldrich Co., LLC (St. Louis, MO, USA). Triethylamine, triethanolamine (TEA), thionyl chloride, methanol, ethanol, isopropanol, toluene, dichloromethane, N,N-dimethylformamide (DMF), Tween 80, hydrochloric acid (HCl), sodium hydroxide, 2-[4-(2-hydroxyethyl)piperazin-1-yl]ethanesulfonic acid (HEPES), glycerol, ethylenediaminetetraacetic acid (EDTA), glutathione, magnesium chloride ($MgCl_2$), dithiothreitol (DTT), trichloroacetic acid (TCA), thiobarbituric acid (TBA), potassium dihydrogen phosphate (KH_2PO_4), hydroxylamine hydrochloride, hydrogen peroxide (H_2O_2), ascorbic acid (AsA), bovine serum albumin (BSA), β-mercaptoethanol, L-methionine, nitroblue tetrazolium (NBT), riboflavin, Triton X-100, polyvinylpyrrolidone (PVP), guaiacol, and acetic acid were acquired from Sinopharm Chemical Reagent Co., Ltd. (Beijing, China). Chromatographic grade acetonitrile and formic acid were purchased from Tedia Company Inc. (Fairfield, OH, USA). The deionized water (18 MΩ/cm) used in the experiment was obtained from a Milli-Q water purification system (Millipore, Milford, MA, USA).

Synthesis of the organosilane-salicylic acid prodrug nanosystem (MSNs-ss-SA)

Synthesis of MSNs-ss-OH

Typically, 0.15 g of TEA and 0.6 g of CTAT were dissolved in 40 mL of deionized water and stirred at 85 °C for 30 min. And then, a mixture of TEOS (3 g) and

BTSPD (1 g) was gradually added under continuous vigorous stirring. After 4 h, the resulting product was collected by centrifugation and refluxed in a 1.5% ammonium nitrate solution for 12 h to remove the CTAT template. This refluxing step was repeated twice, followed by centrifugation, and washing with ethanol. The surfactant-free MSNs-ss-OH were dried under vacuum at 85 °C.

Synthesis of MSNs-ss-NH_2

The synthesized MSNs-ss-OH (500 mg) were dispersed in 100 mL of toluene via ultrasonication. The reaction mixture was heated to 90 °C and stirred for 3 h, followed by the addition of 500 µL of APS. The suspension was then cooled to room temperature and stirred for an additional 1 h. The mixture was reheated to 90 °C and refluxed under nitrogen for 24 h. Afterward, the product was cooled, washed three times with anhydrous ethanol, and dried under vacuum to yield amino-functionalized MSNs-ss-OH (MSNs-ss-NH_2).

Synthesis of salicyl chloride (SAC)

A total of 2.56 g of SA was placed in a single-neck flask equipped with a magnetic stirrer bar. The flask was then purged with nitrogen gas for 20 min to ensure an oxygen-free environment. Thionyl chloride (6.50 mL) was then added to the flask, followed by the slow addition of 6 drops of DMF to catalyze the reaction. Furthermore, the mixture was stirred at 55 °C for 12 h refluxed at 80 °C for 36 h. After cooling the product to room temperature, the remaining thionyl chloride was removed by repeated additions of toluene under vacuum conditions. Finally, a translucent pale-yellow oil was obtained with a yield of 98.81% (2.81 g), which was identified as salicyl chloride. The product did not require further purification and was ready for use in subsequent reactions.

Synthesis of MSNs-ss-SA

To synthesize the MSNs-ss-SA, 0.5 g of MSNs-ss-NH_2 was dispersed in 37.5 mL of toluene (MSNs-ss-NH_2). The dispersion was then purged with nitrogen gas for 30 min to ensure an oxygen-free environment. Afterward, 1.2 mL of triethylamine was added to the mixture. The mixture was then cooled to 0 °C, and a toluene-dichloromethane mixture (v/v, 3:1) solution containing 0.8 g of SAC was added dropwise. After stirring the reaction mixture at room temperature for 48 h, the product was separated by centrifugation. The solid was then washed twice with toluene, followed by multiple washes with ethanol to remove any remaining free SA and triethylamine hydrochloride. The MSNs-ss-SA were obtained by drying under vacuum at 90 °C.

Characterization

The morphological characteristics of the samples were acquired by using a FEI Tecnai 12 transmission electron microscope (TEM) (Philips, Eindhoven, Netherlands) operating at an acceleration voltage of 120 kV. Energy-dispersive X-ray spectroscopy (EDX) was performed on a Tecnai G2 F30 TEM (Philips, Eindhoven, Netherlands) equipped with a 300 kV acceleration voltage for analyzing the elemental composition of the samples. The crystalline phases of the samples were analyzed via powder X-ray diffraction (XRD) using a Bruker D8 Advance diffractometer (Bruker Co. Ltd., Karlsruhe, Germany) with Cu Kα radiation (λ = 1.5418 Å). The functional groups present in the samples were identified by Fourier-transform infrared spectroscopy (FTIR) using a Nicolet iS20 spectrometer (Thermo Fisher Scientific, Waltham, MA, USA) in transmission mode with KBr pellet preparation. The hydrodynamic size and surface charge of the samples were conducted with a Nano-ZS90 Nanosizer (Malvern Instruments, Malvern, UK). The content of SA in the MSNs-ss-SA was quantified using thermogravimetric analysis (TGA) on an SDT-Q600 analyzer (TA Instruments-Waters LLC, New Castle, DE, USA) under a nitrogen atmosphere, with heating from room temperature to 800 °C at a rate of 10 °C/min. X-ray photoelectron spectroscopy (XPS) was performed on a Thermo ESCALAB 250Xi spectrometer (Thermo Fisher Scientific, Waltham, MA, USA) to investigate the elemental composition and chemical states of the samples. Nitrogen adsorption-desorption isotherms at 77 K were measured using a Micromeritics TriStar sorptometer (Micromeritics Instrument Corporation, Norcross, GA, USA) to measure the specific surface area, pore size distribution, and pore volume of the samples. The specific surface area was calculatedusing the Brunauer-Emmett-Teller (BET) method, while the Barrett-Joyner-Halenda (BJH) method was employed to analyze the pore size distribution and pore volume. The chemical structure of the MSNs-ss-SA was further characterized using ^{13}C magic angle spinning nuclear magnetic resonance (^{13}C MAS NMR) spectroscopy on a Bruker AVANCE III 400 WB spectrometer (Bruker BioSpin GmbH, Rheinstetten, Germany) at 400 MHz, with a 4 mm rotor spinning at 6.5 kHz. The concentration of bioavailable silicon in the samples was analyzed by inductively coupled plasma mass spectrometry (ICP-MS; NexION 2000, PerkinElmer, Waltham, MA, USA).

Loading efficiency of SA

Approximately 5 mg of MSNs-ss-OH, MSNs-ss-NH_2, and MSNs-ss-SA were individually placed in platinum pans and heated to 800 °C under a nitrogen atmosphere. The loading efficiency (LE) of SA in MSNs-ss-SA can be

calculated using the following formula based on the TGA results:

$$\mathrm{LE}\ (\%) = (M_3 - M_2) \times\ 100 \tag{1}$$

where M_2 is the weight loss of MSNs-ss-NH_2, and M_3 is the weight loss of MSNs-ss-SA.

Amidase and glutathione-mediated degradation of MSNs-ss-SA

The MSNs-ss-OH containing disulfide bonds can be degraded through reduction reactions with reducing agents, resulting in the formation of thiol-containing organosilicon fragments [45]. Similarly, the amide bonds between SA and amino groups in MSNs-ss-SA can be cleaved by amidase, leading to the release of SA [46]. To investigate the degradation processes of MSNs-ss-SA, TEM was used to observe their breakdown in the presence of 100 U/L amidase and 8.0 mM glutathione. The samples were collected, drop-cast onto Formvar-coated copper grids, dried, and then visualized at predetermined time points (0, 1, 3, 7, 10, and 14 d).

Controlled release kinetics

The release behaviors of SA and bioavailable silicon from MSNs-ss-SA were systematically investigated under various conditions using a dialysis-based method [47]. The prodrug nanosystem was degraded in different solutions at 25 °C to simulate the intracellular environment of rice plants. Typically, a 2.0 mL dispersion containing glutathione (8.0 mM) or amidase (100 U/L) of MSNs-ss-SA was enclosed in a dialysis bag with a molecular weight cutoff of 3500 Da (Thermo Scientific, USA). The dialysis bag was then immersed in 48 mL of deionized water supplemented with either glutathione (8.0 mM) or amidase (100 U/L), and stirred continuously at 100 rpm at room temperature for 14 d. To assess the combined effect of both stimuli, an additional experiment was conducted using a mixed solution of glutathione (8.0 mM) and amidase (100 U/L). At predetermined time points, aliquots were removed from each sample, and an equivalent volume of fresh glutathione or amidase solution was added to maintain consistent experimental conditions. The collected samples were filtered through a 0.22 μm membrane. The released concentrations of SA and bioavailable silicon were quantified using HPLC and ICP-MS, respectively. Deionized water was used without the addition of glutathione or amidase were used to evaluate the baseline release of SA and bioavailable silicon from MSNs-ss-SA. All the experiments were conducted in triplicate.

The release data of SA and bioavailable silicon from MSNs-ss-SA were analyzed using zero-order (2), first-order (3), Higuchi (4), Ritger-Peppas (5), and Weibull (6) models, respectively [48]:

$$\text{Zero-order model}: \frac{M_t}{M_z} = kt \tag{2}$$

$$\text{First-order model}: \frac{M_t}{M_z} = 1 - e^{-kt} \tag{3}$$

$$\text{Higuchi model}: \frac{M_t}{M_z} = kt^{\frac{1}{2}} \tag{4}$$

$$\text{Ritger-Peppas}: \frac{M_t}{M_z} = kt^n \tag{5}$$

$$\text{Weibull model}: \frac{M_t}{M_z} = 1 - \mathrm{e}^{-(\frac{t}{\beta})^k} \tag{6}$$

where M_t is the amount of SA or bioavailable silicon released at time t; M_z is the total amount of SA or bioavailable silicon in the prodrug nanosystem; k is the release constant; and n is the release exponent indicative of the SA or bioavailable silicon release mechanism from MSNs-ss-SA; and β and k are kinetic constants.

Uptake and transportation in rice plants

TEM was used to evaluate the penetration and translocation behaviors of MSNs-ss-SA in rice [49]. At the booting stage of rice, 1.0 mM of MSNs-ss-SA solution was evenly sprayed onto the first fully expanded leaf while ensuring that the droplets did not contact other leaves. The control group was treated with an equal volume of deionized water. After 24 h, the third fully expanded leaf was collected, and small leaf Sect. (1 mm × 2 mm) were excised and fixed in 2.5% glutaraldehyde at 4 °C overnight. The samples were then rinsed with 0.1 mol/L phosphate buffer (pH 7.2) and subsequently fixed with 1% osmium tetroxide. Following fixation, the samples were dehydrated through a graded ethanol series, replaced with acetone, and subsequently infiltrated and embedded in epoxy resin. Ultrathin sections were prepared using an ultramicrotome and placed on copper grids. TEM was used to visualize and image the samples, and the distribution of MSNs-ss-SA in the rice cells was analyzed.

Effects on rice resistance-related physical barriers

Callose staining and content quantification in rice stems

For the histochemical analysis of callose deposition in rice stems, fresh stem segments were fixed in FAA solution (formalin-acetic acid-ethanol) for 24 h. After fixation, the samples were decolorized with 70% ethanol to eliminate chlorophyll, followed by thorough rinsing with distilled water. The decolorized tissues were then stained with 0.05% (w/v) aniline blue prepared in 0.07 M potassium phosphate buffer (pH 9.0) and incubated in the dark for 2 h. Subsequently, the stained samples were mounted on microscope slides and visualized under a fluorescence

microscope (Zeiss Axio Imager M2, Carl Zeiss Microscopy GmbH, Jena, Germany) equipped with UV excitation at 365 nm. Callose deposits were identified by their characteristic bright blue fluorescence. Digital images were captured using an integrated imaging system to evaluate callose deposition levels.

The deposition of callose in the plants was quantified using the method described by Piršelová et al. [50]. To determine the callose content in the rice stems, 0.5 g of stem tissue was collected and incubated in 2 mL of 98% ethanol (v/v) for 1 h. The excess ethanol was removed, and the stems were homogenized in liquid nitrogen. The homogenized tissue was transferred to 5 mL tubes containing 1 mL of 1 M NaOH and incubated at 80 °C for 15 min. After cooling to room temperature, the samples were centrifuged to remove particulates. The callose content was quantified using aniline blue staining, followed by fluorometric measurement with an F-7000 fluorescence spectrophotometer (Hitachi High-Tech Corporation, Tokyo, Japan). Each treatment and control included three independent biological replicates.

Lignin content quantification in rice stems

The content of lignin in rice stems was determined using the method described by Chang et al. [51]. Typically, a total of 10 mg of dried tissue was placed in a test tube, followed by the addition of 1 mL of 25% acetyl bromide in acetic acid. The mixture was heated at 70 °C for 30 min. After cooling to room temperature, 0.9 mL of 2 M NaOH, 5 mL of acetic acid, 0.1 mL of 7.5 M hydroxylamine hydrochloride, and an additional 3 mL of acetic acid were added sequentially. The solution was centrifuged at 1,000 × g for 5 min, and the absorbance of the supernatant was measured at 280 nm to determine the lignin content.

Greenhouse experiment

Rice plants (*Oryza sativa* L. cv. Lemont) were cultivated in sterilized soil in an artificial climate chamber under 30/26°C day/night temperatures, with a photoperiod of 14 h (40,000 lx) and 95 ± 5% relative humidity until the booting stage. The plants were then treated with SA, MSNs-ss-OH, MSNs-ss-OH and SA, or MSNs-ss-SA. Three days after treatment, five tillers per plant were inoculated with *Rhizoctonia solani* (*R. solani*, YN-7). The experimental greenhouse conditions were maintained at 30 °C for the 14 h light period and 28 °C for the 10 h dark period. Lesion length in the rice stems was measured to evaluate the influence of different treatments on rice resistance to sheath blight at 14 d post-inoculation. The experiment was repeated three times, with 20 plants used for each repetition.

RNA isolation and gene expression profile analysis

Approximately 100 mg of fresh rice stems from different treatment groups were collected at 14 d after inoculation with *R. solani*. The stem samples were placed into 2.0 mL centrifuge tubes containing 5 mm shaking beads and immediately frozen in liquid nitrogen. The frozen samples were then ground into a fine powder using a tissue grinder (Shanghai Jingxin, China). Total RNA was extracted using the TRIzol method, and the extracted RNA was reverse-transcribed into cDNA using the HiScript II Q RT SuperMix for qPCR (+ gDNA wiper) kit (Vazyme, China). Quantitative real-time PCR (qRT-PCR) was conducted using the ABI Viia™ 7 Real-Time PCR System (Applied Biosystems, USA) with ChamQ SYBR qPCR Master Mix (Vazyme, China). The sequences of primers used in the analysis were provided in Table S1. The qRT-PCR protocol was as follows: 50 °C for 120 s, 95 °C for 30 s, followed by 40 cycles of 95 °C for 5 s and 60 °C for 30 s. After that, a melting curve analysis was performed with the following steps: 95 °C for 15 s, 60 °C for 60 s, and 95 °C for 15 s. *eEF1α* was used as the housekeeping gene, and the relative expression levels of target genes were calculated using the $2^{-\Delta\Delta CT}$ method. Each sample was analyzed with three biological replicates and three technical duplications.

Phytohormone extraction and analysis

Fourteen days after inoculation with *R. solani*, 0.15 g of fresh rice stem tissue was transferred into a 2 mL centrifuge tube. Four 5 mm shaking beads were added to each tube, followed by immediate freezing in liquid nitrogen. The samples were subsequently ground into a fine powder using a TissueLyser (Jingxin, Shanghai, China). After homogenization, 1 mL of extraction solution (isopropanol: H_2O: HCl = 2:1:0.002) was added, and the mixture was sonicated for 30 min at 4 °C in the dark using a KQ5200DE ultrasonic cleaner (Kunshan Shumei Ultrasonic Instruments, Suzhou, China). The samples were centrifuged at 15,000 rpm for 2 min at 4 °C using an Eppendorf 5424R centrifuge (Eppendorf SE, Hamburg, Germany), and the resulting supernatant was subjected to HPLC-MS/MS analysis. All analyses were conducted using a 1260 Agilent Technologies system (Agilent Technologies Inc., Santa Clara, CA, USA) equipped with a binary pump and vacuum degasser, and a Varian 410 Prostar autosampler (Varian Inc., Palo Alto, CA, USA) with a 10 µL injection loop. The system was coupled to a Thermo Scientific TSQ-4600 triple quadrupole mass spectrometer (Thermo Fisher Scientific, Waltham, MA, USA). HPLC separation was performed using a Phenomenex Kinetex F5 (100 × 2.1 mm, 2.6 µm) (Phenomenex Inc., CA, USA) at a flow rate of 0.2 mL/min, with the column temperature maintained at 40 °C using an Agilent column thermostat. The mobile phases

consisted of solvent A (H_2O containing 0.1% formic acid) and solvent B (acetonitrile). The HPLC gradient program was as follows: 0–1 min, 90% A; 1–6 min, 90 to 45% A; 6–8 min, 45 to 0% A; 8–10 min, 0% A; 10–11 min, 0–90% A; 11–15 min, 90% A. Samples were ionized using an electrospray ionization (ESI) source in negative ion mode. SA and JA were quantified using multiple reaction monitoring (MRM). The fragment ion m/z values were 137.1/93.1 and 209.1/59.2. Argon was used as the collision gas, with the pressure set to 2 mbar for all the experiments. Hormone levels were quantified from three independent biological replicates for each treatment.

Antioxidative activity

Fresh stem tissue (0.2 g) was homogenized at 60 Hz for 30 s using a tissue grinder. After homogenization, enzyme extraction buffer was added, and the mixture was vortexed for 15 s. The enzyme extraction buffer consisted of HEPES buffer (pH 7.8) supplemented with 20% (v/v) glycerol, 1 mM EDTA, 1 mM AsA, 1 mM glutathione, 5 mM $MgCl_2$, and 1 mM DTT. The homogenate was centrifuged at 10,000 × g for 20 min at 4 °C, and the resulting supernatant was collected for subsequent analysis. For the malondialdehyde (MDA) assay, 4 mL of a TCA-TBA solution was mixed with 2 mL of the enzyme extract. For the control, 2 mL of extraction buffer was used instead of the enzyme extract. The reaction mixture was incubated in boiling water for 20 min and cooled to room temperature. The cooled mixture was centrifuged at 4,000 × g for 10 min, and the supernatant was collected. The absorbance of the supernatant was measured at 450, 532, and 600 nm using a spectrophotometer. Catalase (CAT) was extracted using 25 mM KH_2PO_4 buffer (pH 7.4). The reaction mixture consisted of 100 µL of supernatant and 1,900 µL of 10 mM H_2O_2. The reaction was monitored at 240 nm for 3 min, and the decrease in absorbance was recorded. The extinction coefficient of H_2O_2 was set as 23.148 mM^{-1} cm^{-1}, and the CAT activity was expressed accordingly. SOD was extracted using 50 mM phosphate buffer (pH 7.8) containing 0.1% (w/v) ascorbate, 0.1% (w/v) BSA, and 0.05% (w/v) β-mercaptoethanol. Superoxide dismutase (SOD) activity was determined indirectly via the inhibition of NBT reduction. The reaction mixture contained 100 µL of enzyme extract, 1,900 µL of 50 mM phosphate buffer (pH 7.8), 9.9 mM L-methionine, 57 µM NBT, 0.0044% riboflavin, and 0.025% Triton X-100. The mixture was exposed to fluorescent light at 250 µmol m^{-2} s^{-1} for 20 min, and the absorbance was measured at 560 nm to determine SOD activity. Peroxidase (POD) was extracted using a 50 mM phosphate buffer (pH 7.0) containing 1% (w/v) PVP. The reaction mixture consisted of 50 µL of enzyme extract, 1.75 mL of 50 mM sodium phosphate buffer (pH 7.0), and 0.1 mL of 4% guaiacol. The reaction was initiated by adding 0.1 mL of 1% (v/v) H_2O_2. The increase in absorbance at 470 nm was recorded over 2 min to calculate POD activity.

Safety assessment

Phytotoxicity on Oryza sativa seedlings

Typically, five uniformly germinated *Oryza sativa* L. cv. Lemont seeds were transferred to a plastic box (5.1 cm×6.4 cm×6.45 cm) filled with sterilized paddy soil. When the rice seedlings reached the three-leaf stage, the leaves were treated with different concentrations of MSNs-ss-SA (1.0, 2.0, 4.0 and 8.0 mM). Each treatment was replicated six times, with a control group treated with distilled water. The plants were then cultivated in an automatic illuminating incubator at 28 °C, and 70% relative humidity, with a 12-h light/12-h dark photoperiod. Seven days after treatment, key growth and physiological parameters were measured to determine the phytotoxicity of MSNs-ss-SA to *Oryza sativa* seedlings.

Acute toxicity to Daphnia magna neonates

Daphnia magna is highly sensitive to aquatic toxicants, which is recognized as an internationally standardized indicator organism for evaluating the ecological safety of nanomaterials in aquatic environments [52]. The acute toxicity of SA to *Daphnia magna* neonates (< 24 h old) was measured according to the Organization for Economic Cooperation and Development (OECD) standard procedure [53]. Various concentrations of SA and MSNs-ss-SA (0, 0.0625, 0.125, 0.25, 0.5, 1.0, 2.0, 4.0 and 8.0 mM) solutions were prepared. Ten neonates were placed in 70 mm diameter glass Petri dishes containing 10 mL of the prepared solutions. The concentrations were standardized based on the SA content in both SA technical and MSNs-ss-SA. The organisms were not fed during the experiment. Neonates were exposed for 48 h at 20 ± 2 °C with a 16:8 h light-to-dark cycle. At the end of the exposure period, the mortality rate was determined by counting the number of deceased neonates in each Petri dish. Each treatment was replicated three times. The median lethal concentration (LC_{50}) for the 48-h exposure was calculated using probit analysis.

Acute toxicity to Eisenia fetida

Eisenia fetida, an important bioindicator for soil health, is highly sensitive to soil pollutants [54]. The acute toxicity of SA and MSNs-ss-SA to *Eisenia fetida* was evaluated using standard artificial soil tests [55]. The sandy artificial soil was composed of 10% ground sphagnum peat, 20% kaolin clay, and 70% industrial fine sand. The SA and MSNs-ss-SA were incorporated into 500 g of this soil to create treatments with different active ingredient concentrations (50, 100, 200, 400, 800, 1600, and 3200 mg/kg). The soil moisture content was adjusted to 35% of its maximum water-holding capacity. The SA

content in both SA technical and MSNs-ss-SA was standardized based on the mass of SA. The treated soils were placed into 1 L glass beakers, and ten pre-acclimated earthworms were introduced into each beaker. The control group was treated with an equal volume of deionized water. The beakers were sealed with perforated polyvinyl chloride polymer film and maintained at 20 ± 2 °C with 80-85% relative humidity and 400–800 lx light intensity. After 14 d, mortality was recorded, and the LC_{50} for *Eisenia fetida* was calculated using log-probit analysis.

Apoptosis assay in human hepatocyte L02 cells

To evaluate the cytotoxicity of MSNs-ss-SA, apoptosis in human hepatocyte L02 cells was quantified via flow cytometry. Cells in the logarithmic growth phase were seeded into 6-well plates at a density of 1×10^5 cells/mL and cultured for 24 h. Subsequently, cells were treated for 24 h with free SA (1.0 mM), MSNs-ss-SA (1.0 mM SA equivalent), or DMEM medium (untreated control). After treatment, cells were washed three times with ice-cold PBS, detached using trypsin, and centrifuged at for 5 min. Cell pellets were resuspended in 100 µL of binding buffer and stained with 5 µL Annexin V-FITC and 10 µL propidium iodide (PI) in the dark for 15 min, with gentle resuspension every 5 min. Apoptotic profiles were analyzed using a BD FACSCalibur flow cytometer (BD Biosciences, San Jose, CA, USA), and data were processed with FlowJo v10 software. Quadrants were defined as follows: necrotic cells (Annexin V^-/PI^+, Q1), late-stage apoptotic cells (Annexin V^+/PI^+, Q2), early apoptotic cells (Annexin V^+/PI^-, Q3), and viable cells (Annexin V^-/PI^-, Q4).

Effects on rice yield and quality

Grain yield and yield components

The field experiment was conducted from May 2024 to November 2024 at the College of Agriculture, Yangzhou University (32°34′N, 119°40′E). Field trials were conducted in a humid subtropical monsoon climate, with an average annual temperature of 14.8 °C, average annual precipitation of 1262.2 mm, and a frost-free period of approximately 220 d. The physicochemical properties of the paddy soil (0–20 cm) were as follows: pH 6.87, organic matter content of 12.6 g/kg, total nitrogen content of 9.4 g/kg, available nitrogen content of 73.3 mg/kg, available phosphorus content of 85.6 mg/kg, and available potassium content of 103.1 mg/kg.

To evaluate the potential of MSNs-ss-SA for agricultural applications, two rice varieties with different levels of resistance to sheath blight were selected for this study. The highly susceptible indica variety *Oryza sativa* L. cv. Lemont and the highly resistant japonica variety *Oryza sativa* L. cv. Huruan 1212 were chosen to evaluate the effects of MSNs-ss-SA on rice quality and yield. Basal fertilizer was applied 7 d before transplanting rice seedlings, which consists of 235 kg/ha urea, 750 kg/ha superphosphate, and 300 kg/ha potassium chloride. Nitrogen supplementation was applied at the tillering, jointing, and panicle differentiation stages, with 118 kg/ha of urea administered at each stage to ensure adequate nitrogen availability. Irrigation and pest management were in accordance with standard local practices.

Seedlings at the 3.5-leaf stage were transplanted with a row spacing of 28 cm × 12 cm. Each experimental plot covered an area of 30 m^2, and the treatments were arranged in a randomized block design with three replicates per treatment. Sowing occurred on May 23, transplanting on June 16, and harvesting occurred on November 15. During the booting stage of the rice plants, the rice leaves were treated with different concentrations of MSNs-ss-SA (0.1, 1.0, and 4.0 mM), which were based on the concentration of SA. At maturity, 50 rice hills per treatment were systematically surveyed using a combination of fixed-point and random sampling methods. The number of panicles per hill was recorded and categorized to evaluate yield components. Key agronomic traits, including grains per panicle, seed-setting rate, thousand-grain weight, and total yield, were systematically measured and recorded. The control group was treated with a 0.25% Tween 80 solution without MSNs-ss-SA.

Grain quality

The grains were stored at room temperature for three months before evaluating their quality attributes. Rice processing, and nutrition were assessed using standardized methodologies [56]. Processing quality parameters, including the brown rice rate, milled rice rate, head rice rate, chalky grain rate, and chalkiness degree, were evaluated using conventional milling techniques and image analysis. The brown rice and milled rice rates were determined by calculating the percentage of dehulled and polished rice relative to the total grain weight. The head rice rate was measured as the proportion of intact kernels (≥ 75% of the original grain length) in the milled rice. The chalky grain rate and chalkiness degree were quantified using a chalkiness scanner (SC-E Rice Chalkiness Meter, Wanshen, Hangzhou, China) to assess both the proportion and intensity of chalkiness in the rice grains. The protein content was measured using the Kjeldahl method, whereas the amylose content was analyzed via iodine colorimetry [57, 58].

Data analysis

All the statistical analyses were conducted using SPSS 23.0 statistical analysis software (SPSS, Chicago, IL, USA). The data were analyzed by the Duncan multiple range test ($p < 0.05$) and expressed as the mean ± standard deviation (SD) for all the experiments.

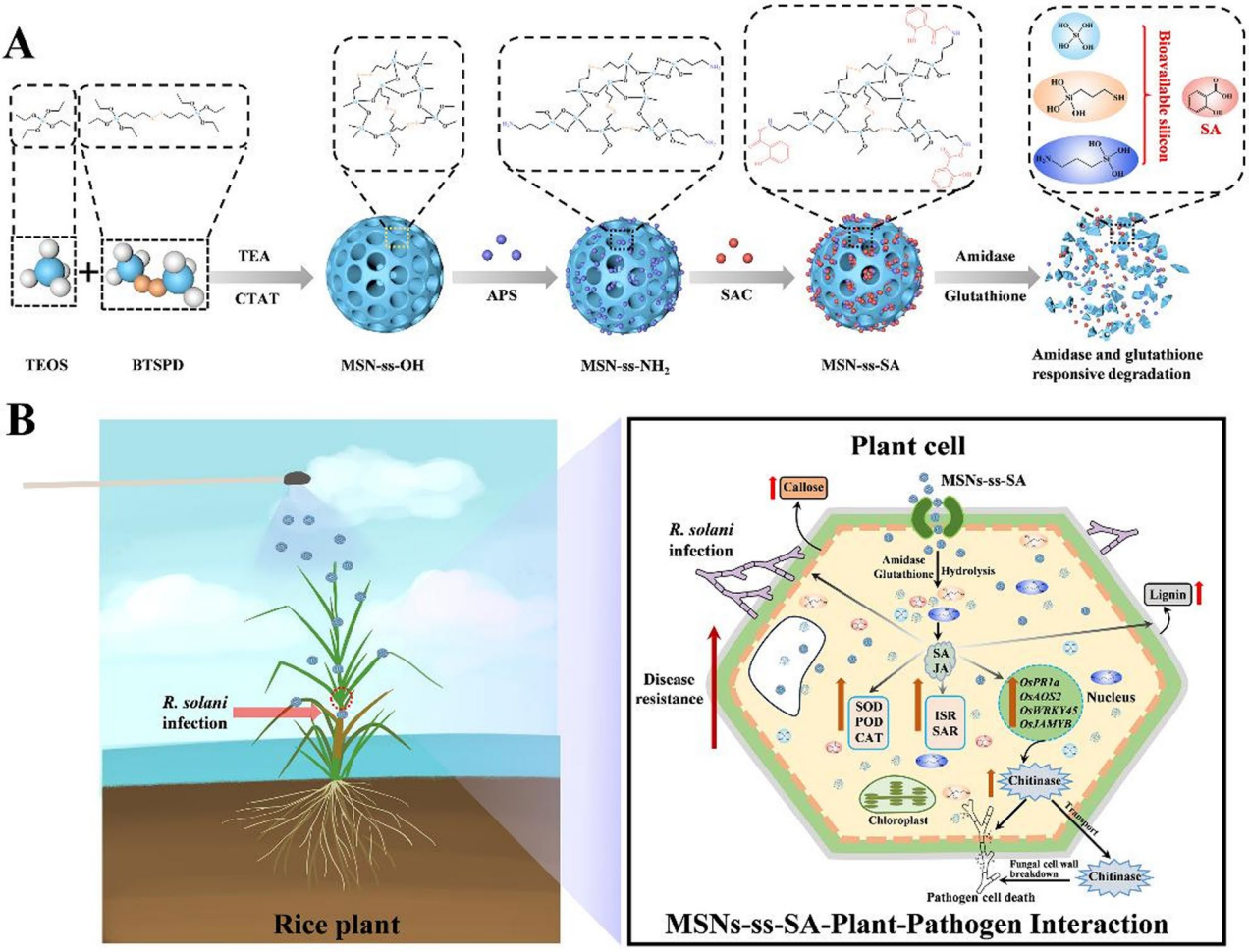

Fig. 1 The synthesis processes of MSN-ss-SA and the mechanism for the controlled release of SA and bioavailable silicon from MSN-ss-SA (**A**). The proposed mechanistic model for the MSNs-ss-SA-plant-pathogen interaction in the suppression of rice sheath blight (*R. solani*) (**B**)

Results and discussion

Preparation and characterization of MSNs-ss-SA

The detailed synthesis processes of MSN-ss-SA are illustrated in Fig. 1A. First, SAC was synthesized via the reaction of SA with thionyl chloride, activating the carboxyl group for subsequent chemical modifications. And then, the disulfide-bridged mesoporous silica nanoparticle (MSN-ss-OH) was prepared via a hydrothermal method, using TEOS and BTSPD as silane sources, CTAT served as the template, and TEA as the catalyst. After removing the surfactant (CTAT) in the channels of MSN-ss-OH, the surface and pores were aminated by reaction with APS, resulting in an amine-functionalized MSN-ss-OH (MSN-ss-NH_2). Finally, the amino groups were conjugated with SAC by a nucleophilic substitution reaction, forming a bioavailable silicon-based prodrug nanosystem (MSN-ss-SA). As illustrated in Fig. 2A, the MSNs-ss-OH exhibited a uniform spherical morphology with distinct mesoporous structures. At higher magnification in the TEM image, a well-defined central radial pore structure was clearly observed (Fig. 2D). After the modification with amino groups on the surface of MSNs-ss-OH, the TEM images showed that the mesoporous channels were partially obscured by those functional organic compounds (Fig. 2B and E). After loading with SA, the pore structure of the MSNs-ss-SA became undetectable, which may be due to the entrapment of pesticide molecules within the channels and on the surface of MSNs-ss-NH_2 (Fig. 2C and F). The average sizes of MSNs-ss-NH_2 and MSNs-ss-SA were 89.0 and 90.7 nm respectively, both of which are larger than the size of the blank MSNs-ss-OH (86.5 nm). The averaged hydrodynamic sizes of MSNs-ss-OH, MSNs-ss-NH_2, and MSNs-ss-SA, determined by dynamic light scattering (DLS) measurements, were 161.1, 181.5 and 254.2 nm respectively (Table S2). The Z-average size was increased in each step, particularly after the formation of MSNs-ss-SA, which is a sign for addition of SA. The size differences between the TEM and DLS measurements can be partly attributed to the larger hydrodynamic radius of the particles measured in

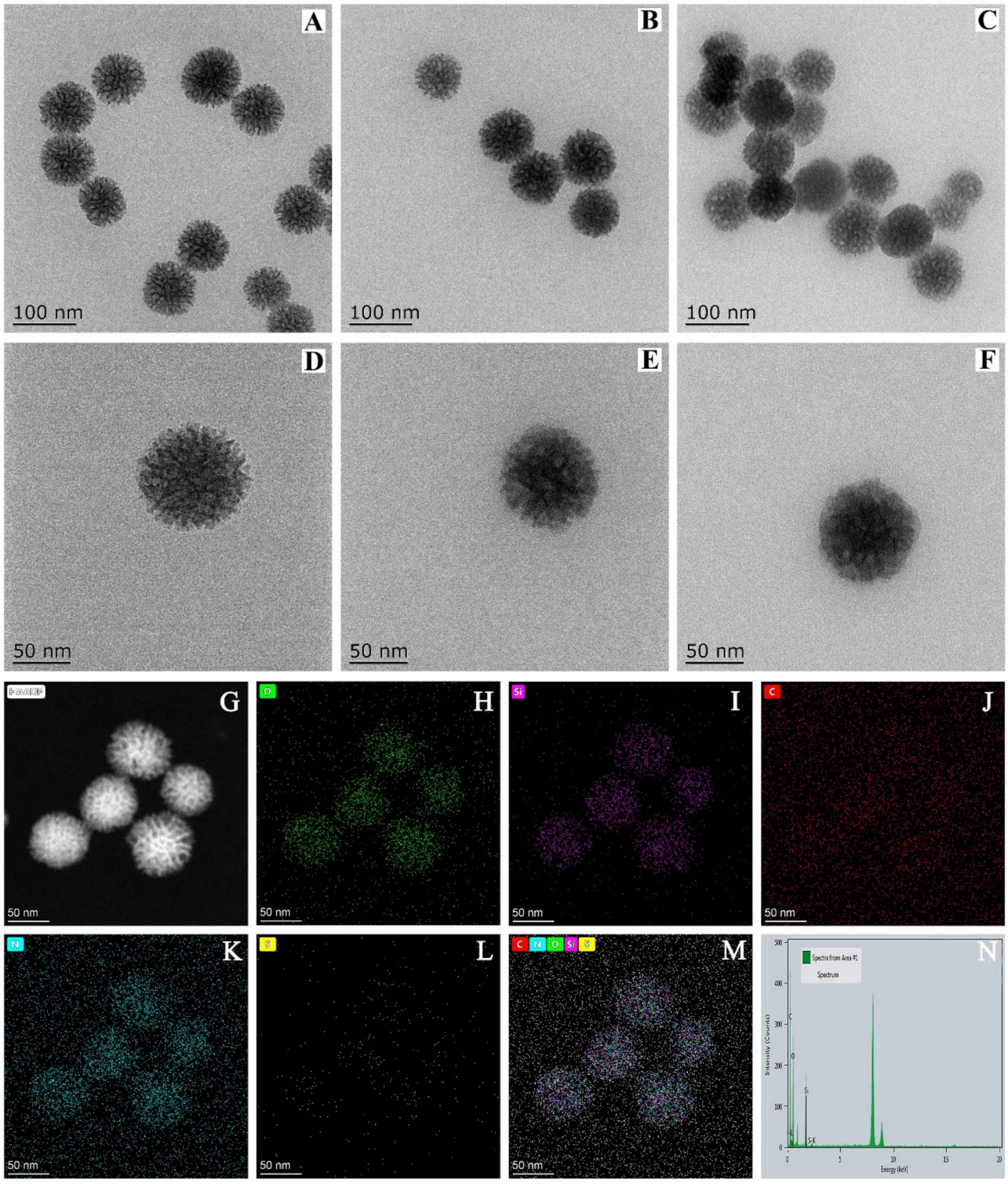

Fig. 2 TEM images of MSNs-ss-OH (**A**), MSNs-ss-NH_2 (**B**) and MSNs-ss-SA (**C**); The images of (**D**), (**E**) and (**F**) were higher magnification of TEM images of (**A**), (**B**) and (**C**); Element mapping (**G**–**M**) of MSNs-ss-SA; EDX spectrum of MSNs-ss-SA (**N**)

solution by DLS [59]. Some additional aggregation effects may have also contributed to the increased size observed in DLS measurements [60]. TEM mapping (Figs. 2G-M) and EDX spectrum (Fig. 2N) further suggested that the O, Si, C, N, and S elements were uniformly distributed in the MSNs-ss-SA. The solid-state ^{13}C MAS NMR spectrum of MSNs-ss-SA (Fig. S1) revealed resonances at 43.23, 22.23, and 11.02 ppm, corresponding to the -CH_2

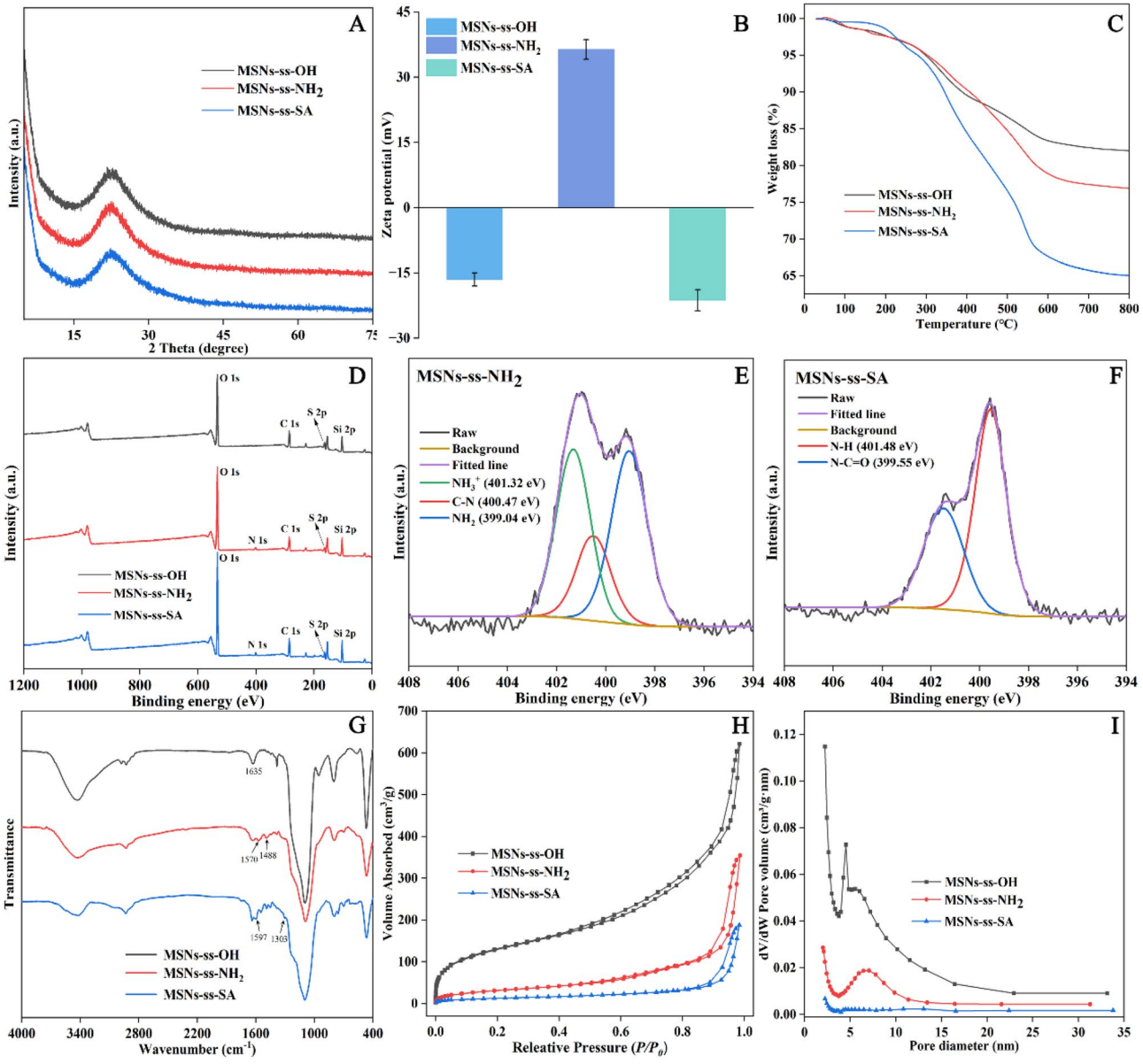

Fig. 3 XRD patterns of MSNs-ss-OH, MSNs-ss-NH2, and MSNs-ss-SA (**A**); Zeta potential of MSNs-ss-OH, MSNs-ss-NH2, and MSNs-ss-SA (**B**); TGA analysis of MSNs-ss-OH, MSNs-ss-NH2, and MSNs-ss-SA (**C**); Survey scan XPS spectra of MSNs-ss-OH, MSNs-ss-NH2, and MSNs-ss-SA (**D**); Deconvolution of high-resolution XPS spectra for the N 1s peaks of MSNs-ss-NH2 (**E**); Deconvolution of high-resolution XPS spectra for the N 1s peaks of MSNs-ss-SA (**F**); FTIR spectra of MSNs-ss-OH, MSNs-ss-NH2, and MSNs-ss-SA (**G**); Nitrogen adsorption–desorption isotherms of MSNs-ss-OH, MSNs-ss-NH2, and MSNs-ss-SA (**H**); Pore size distribution of MSNs-ss-OH, MSNs-ss-NH2, and MSNs-ss-SA (**I**)

groups in the structure of MSNs-ss-SA [61]. Additionally, the characteristic peaks at 170.98 and 161.83 ppm were attributed to the carbonyl carbon in the amide bonds and the carbon of the benzene ring linked to a hydroxyl group respectively, indicating the successful grafting of SA onto MSNs-ss-NH_2 via amide bonds [62]. Furthermore, the changes in the physical and chemical properties of MSNs-ss-SA during synthesis were systematically investigated. As shown in Fig. 3A, the XRD pattern of MSNs-ss-OH exhibited a broad peak at approximately $2\theta = 22.3°$, with no discernible diffraction peaks, confirming its amorphous structure [63]. A comparison with the JCPDS file for pure silica nanoparticles indicated that the synthesized MSNs-ss-OH did not contain any impurity peaks [64]. The introduction of amino groups and SA did not alter the diffraction pattern of MSNs-ss-OH, indicating that the modification process preserved the structural integrity of the prodrug nanosystem. The zeta potential variations of the prodrug nanosystem were also measured and shown in Fig. 3B. The zeta potential of MSNs-ss-OH was – 16.5 mV, which was attributed to the negative charge of the Si-OH groups on their surface. For

MSNs-ss-NH_2, the zeta potential was increased to + 36.4 mV due to the replacement of Si-OH with C-NH_2 groups [33]. When SA was grafted onto MSNs-ss-NH_2, the zeta potential was reversed to – 21.3 mV, reflecting the shielding effect of the phenolic hydroxyl groups in SA [65]. Furthermore, the SA loading capacity of the prodrug delivery system was determined by TGA analysis. As depicted in Fig. 3C, the weight loss of MSNs-ss-OH was 18.0%, which was attributed to the decomposition of organic compounds and the evaporation of water molecules. After APS modification, the weight loss of MSNs-ss-NH_2 was increased to 23.1%. Following chemical coupling with SA, the weight loss was further increased to 35.1%. Based on more weight loss of MSNs-ss-SA compared with MSNs-ss-NH_2, the loaded amount of SA was calculated to be 12.0% in the MSNs-ss-SA. To further investigate the changes in elemental composition and electronic states of MSNs-ss-OH during chemical modification, XPS analysis was performed [66]. As illustrated in Fig. 3D, the survey spectrum of MSNs-ss-OH presented characteristic peaks at 103.4, 164.42, and 285.39 eV, corresponding to Si 2p, S 2p, and C 1s, respectively. Following the grafting of APS, a new nitrogen peak at 401.23 eV confirmed the successful formation of MSNs-ss-NH_2. High-resolution N 1s XPS spectra of MSNs-ss-NH_2 and MSNs-ss-SA further confirmed the nature of the nitrogen species (Fig. 3E and F). MSNs-ss-NH_2 exhibited three characteristic peaks at 401.32, 400.47, and 399.04 eV, which correspond to NH_3^+, C-N, and NH_2, respectively [67]. In contrast, MSNs-ss-SA showed two peaks at 401.48 and 399.55 eV, corresponding to N-H and N-C = O, respectively [68]. These results indicated that SA was successfully grafted onto MSNs-ss-NH_2 via amide bonds (Fig. 3F). The chemical modification processes of MSNs-ss-OH were further characterized using FTIR spectroscopy (Fig. 3G). Compared to the MSNs-ss-OH, MSNs-ss-NH_2 displayed two characteristic peaks at approximately 1488 and 1570 cm^{-1}, corresponding to N-H stretching and bending vibrations respectively, indicating the successful introduction of amino groups [69]. After the conjugation of SA, a new peak at 1597 cm^{-1} was observed, which was attributed to the C = C stretching vibration of the benzene ring [70]. In addition, a peak at 1303 cm^{-1} was assigned to C-OH (phenolic) stretching, indicating the successful attachment of SA to MSN-ss-NH_2 [71]. The variation of surface area and average pore size during the process of modification were also monitored by N_2 adsorption-desorption isotherms (Fig. 3H and I, Table S2). The bare MSNs-ss-OH exhibited the typical type IV isotherm, with a BET surface area of 460.97 m^2/g, a pore volume of 1.07 cm^3/g, and an average pore size of 9.34 nm. After amino modification, the BET surface area of MSNs-ss-NH_2 was significantly decreased to 115.48 m^2/g, with a pore volume reduction to 0.61 cm^3/g. Further decreases were observed for MSNs-ss-SA, indicating successful loading of SA for MSNs-ss-NH_2.

Release kinetics

Controlled release of SA

As shown in Fig. 4A, a small amount of SA (6.50%) was released from MSNs-ss-SA over a period of 14 d in the absence of glutathione and amidase, suggesting that SA was primarily anchored onto the MSNs-ss-NH_2 by chemical grafting. The cumulative release of SA in 8.0 mM glutathione rose to 49.84% over 14 d, which could be attributed to the susceptibility of the disulfide bonds within the MSNs-ss-SA framework to cleavage under reductive microenvironment conditions, resulting in the structural disintegration of MSNs-ss-SA and the significant release of the loaded SA [72]. With the introduction of amidase into the MSNs-ss-SA dispersion, the release of SA from MSNs-ss-SA exhibited a significant acceleration, achieving a cumulative release of 91.30% within 14 d. More importantly, under the combined influence of glutathione and amidase, the release rate of SA was further enhanced. This was primarily attributed to the erosion of the MSNs-ss-SA scaffold and the cleavage of amide bonds, indicating its dual-responsive performance to both redox and amidase stimuli, which enables the controlled release of SA.

Controlled release of bioavailable silicon

As shown in Fig. 4B, in the absence of glutathione, only 8.29% cumulative release of bioavailable silicon in amidase solution was observed, whereas in the presence of glutathione, 67.41% of bioavailable silicon was released over 14 d. Compared with amidase-treated MSN-ss-SA, glutathione treatment significantly enhanced the release rate of bioavailable silicon. Further investigation into the combined effect of amidase and glutathione on the release rate of bioavailable silicon revealed that, under both stimuli, the release rate was significantly accelerated, with 70.51% of bioavailable silicon released after 14 d. This was primarily attributed to the cleavage of amide bonds in MSNs-ss-SA, which increased the hydrophilicity of the carriers, thereby accelerating the degradation of disulfide bonds in the MSN-ss-OH by glutathione and promoting the release of bioavailable silicon [73].

The release mechanism

To further investigate the release mechanism of MSNs-ss-SA, the release kinetics of SA and bioavailable silicon were analyzed using zero-order, first-order, Higuchi, Ritger-Peppas, and Weibull models. The parameters and regression coefficients (r^2) of each model are shown in Tables S3-S4. The release of SA was well-described by the Weibull model under various conditions (Table S3), with regression coefficients consistently >0.997. The diffusion

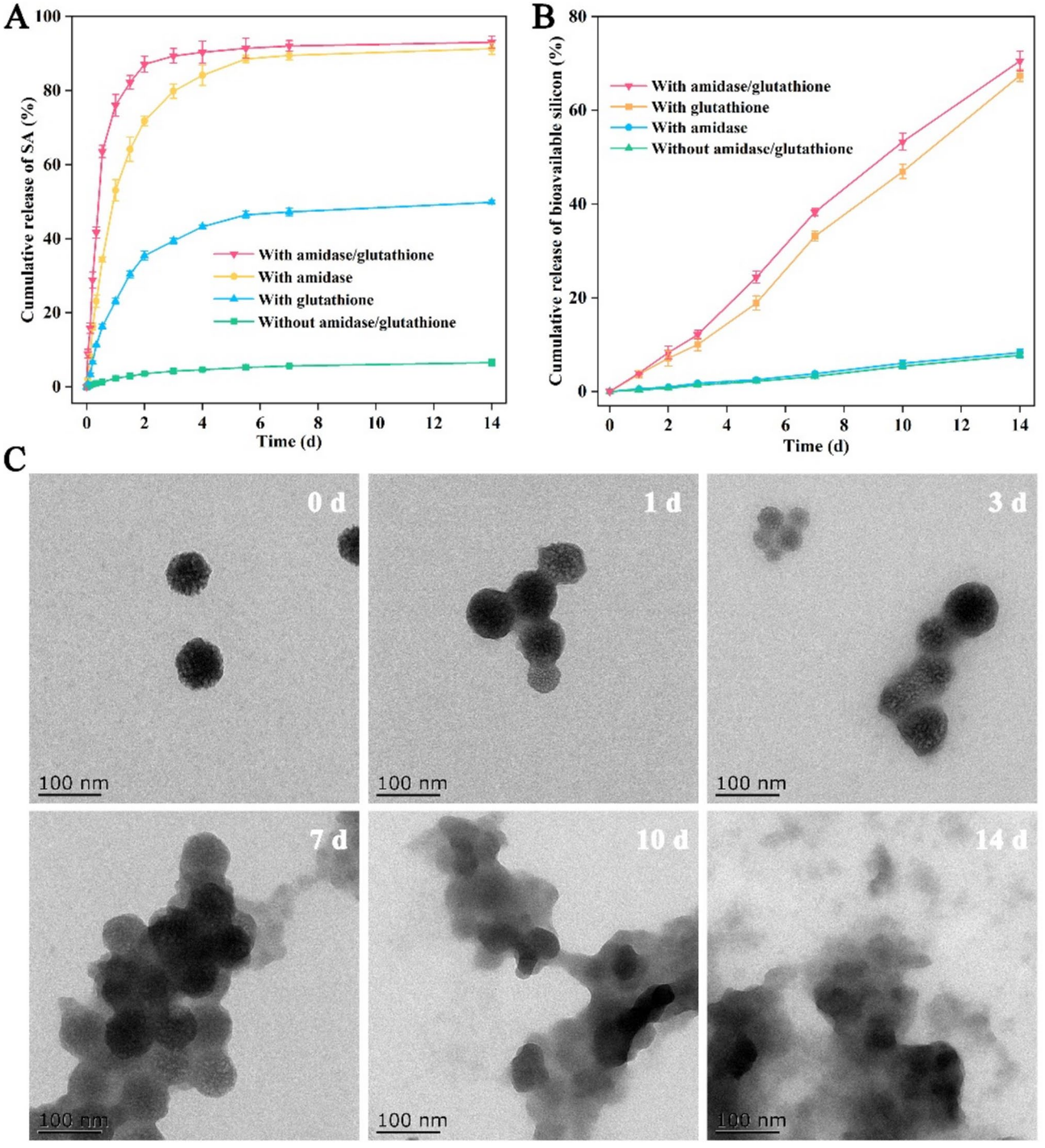

Fig. 4 Release profiles of SA from MSNs-ss-SA in the presence of glutathione and amidase (**A**); Release profiles of bioavailable silicon from MSNs-ss-SA in the presence of glutathione and amidase (**B**); In *vitro* degradation of MSNs-ss-SA in a mixture solution containing 8.0 mM glutathione and 100 U/L amidase (**C**)

index values for MSNs-ss-SA were all <1.0, indicating that the release of SA follows an anomalous diffusion mechanism [74]. In contrast, the release of bioavailable silicon was best fitted to the Ritger-Peppas model (Table S4), which produced significantly higher regression coefficients (r^2 > 0.994), demonstrating a strong alignment with the experimental release profiles. Moreover, the diffusion index values for MSNs-ss-SA were all >0.89, suggesting that the bioavailable silicon release was primarily attributed to erosion of the framework [75].

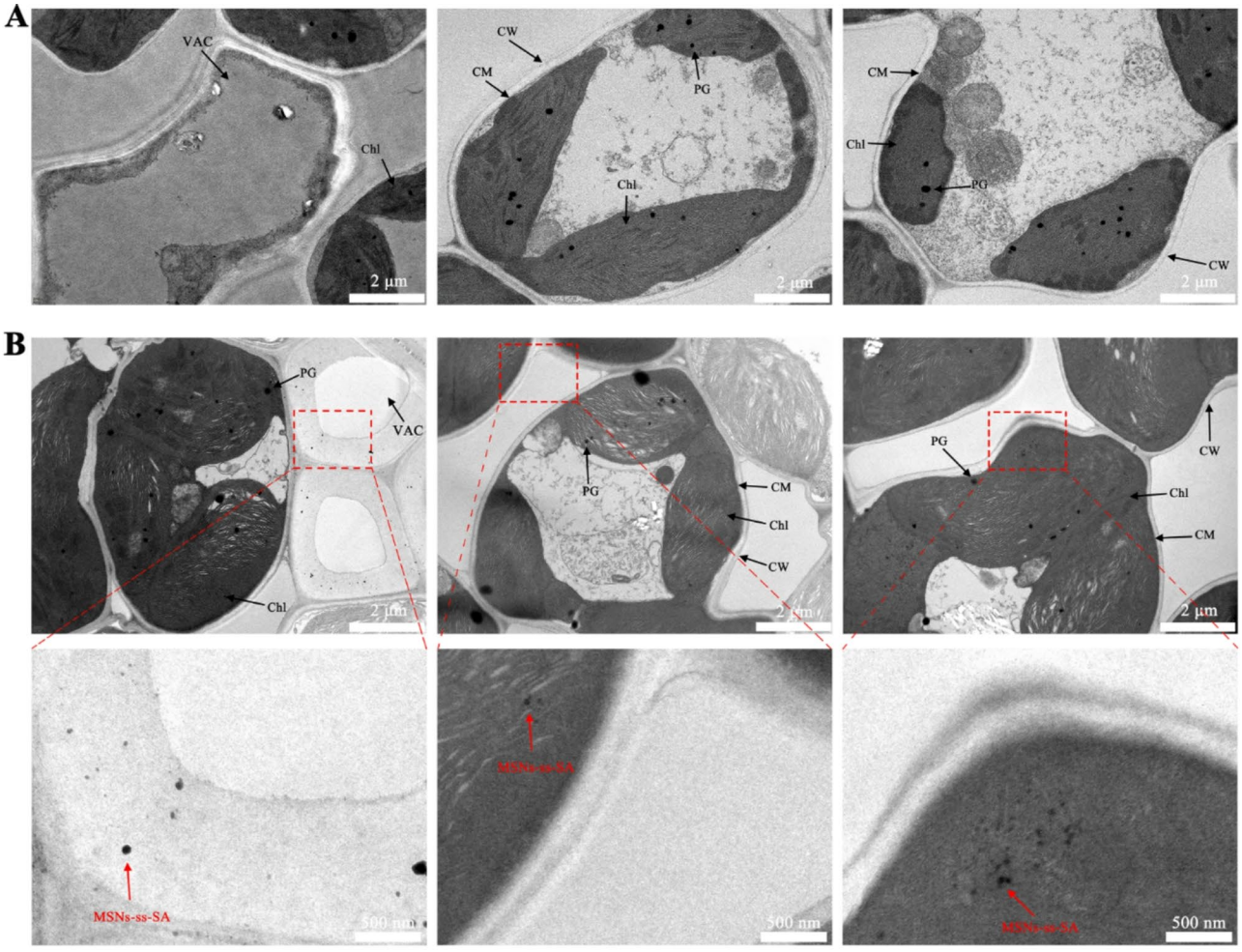

Fig. 5 TEM images of rice leaves after treatment with deionized water (A) and MSN-ss-SA (B). Red arrows indicate the localization of MSNs-ss-SA. Abbreviations: Chl refers to chloroplast; VAC refers to vacuole; CM refers to cell membrane; CW refers to cell wall; and PG refers to protoplasmic granule vesicles

In *vitro* biodegradation

As shown in Fig. 4C, the MSN-ss-SA framework began to disintegrate after one day of incubation under amidase and glutathione conditions. As the time went on, progressive dissolution of certain nanoparticles was observed, with significant degradation noted by day 7. Following exposure to an 8.0 mM glutathione and 100 U/L amidase mixture solution for 14 d, the MSN-ss-SA framework was almost entirely eroded, and no intact spherical nanoparticles were observed. This finding suggested that the free thiol groups in glutathione effectively cleave the disulfide bonds within the framework, thereby facilitating the degradation of the MSN-ss-SA structure and promoting the release of SA and bioavailable silicon.

Uptake and translocation in rice plants

As depicted in Fig. 5A, rice leaf cells treated with deionized water maintained intact and well-preserved cellular structures, including clearly defined cell walls (CW), cell membranes (CM), chloroplasts (Chl), and protoplast granules (PG), with no detectable MSNs-ss-SA. In contrast, the TEM images in Fig. 5B revealed the intracellular distribution of MSNs-ss-SA within rice leaf cells. The treated cells retained structural integrity, with MSNs-ss-SA primarily localized in vacuoles (VAC), cell walls (CW), and chloroplasts (Chl). Furthermore, after being sprayed on the upper leaves, MSNs-ss-SA was detected in the lower leaves, indicating its high penetration efficiency and rapid translocation capacity in rice plants. These findings demonstrated that MSNs-ss-SA could efficiently penetrate rice cell walls and achieve targeted localization within cellular organelles. This efficient translocation significantly enhanced the utilization of SA and bioavailable silicon within the rice plants, thereby inducing SAR throughout the plant [76, 77].

Effects on induced resistance in rice plants

As illustrated in Fig. 6, lesion lengths were measured 14 d after inoculation. The results demonstrated that at an SA concentration of 0.1 mM, none of the treatments

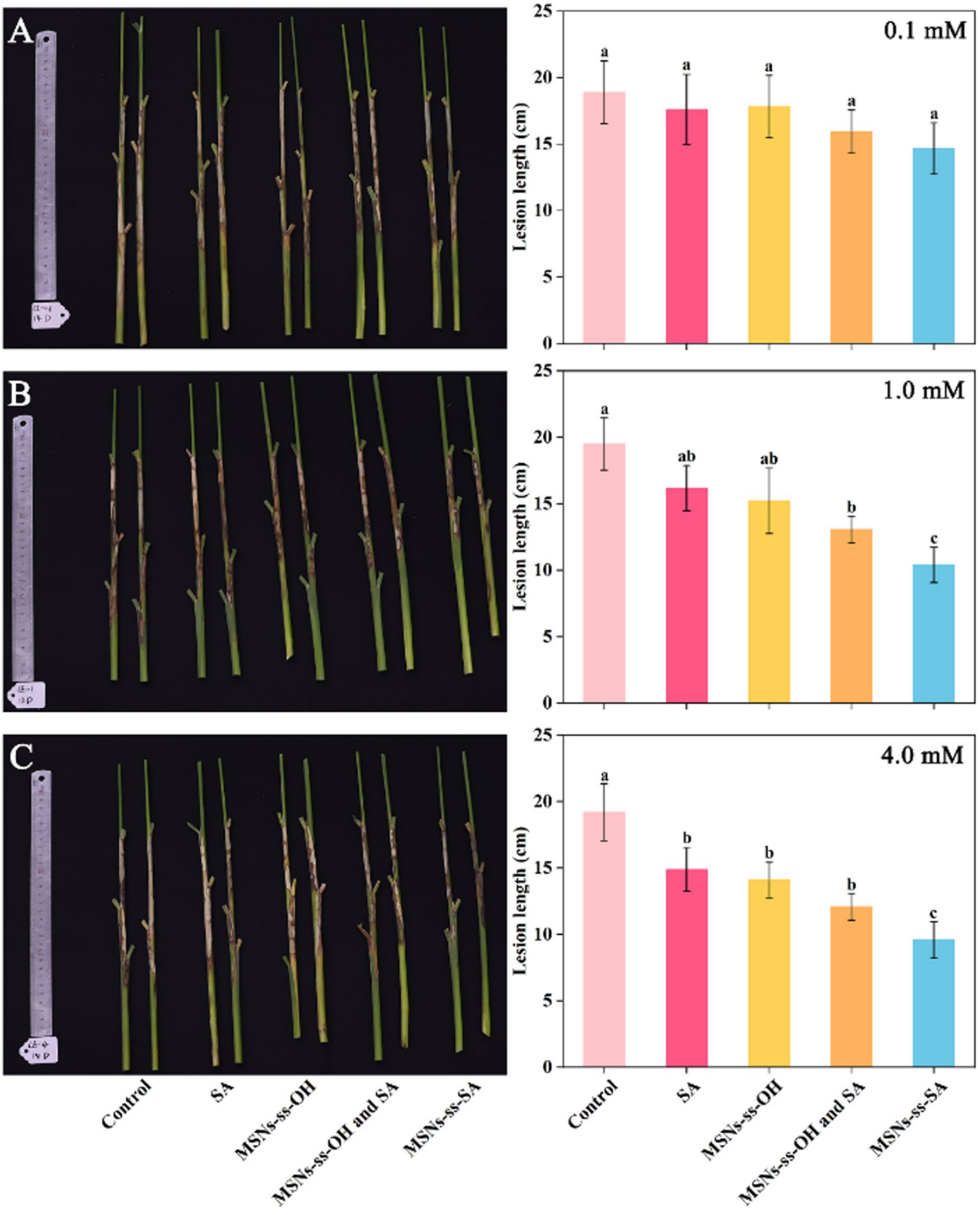

Fig. 6 Images of disease severity and statistical histogram of lesion length in the rice cultivar Lemont. Rice plants at the booting stage were treated with SA, MSNs-ss-OH, MSNs-ss-OH and SA, or MSNs-ss-SA, followed by inoculation with the sheath blight pathogen (*R. solani*) three days post-treatment. Treatments were performed with SA concentrations of 0.1 mM (**A**), 1.0 mM (**B**), and 4.0 mM (**C**). Error bars represent SD and different capital letters represent significant differences ($p < 0.05$)

significantly induced resistance to sheath blight in rice. In contrast, at higher concentrations of 1.0 mM and 4.0 mM, the MSNs-ss-SA treatment resulted in 46.67% and 50.09% reduction in lesion length, respectively, compared with those of the control treatment. These findings indicate that the MSNs-ss-SA treatment had a greater ability to induce resistance to sheath blight in rice plants compared with the other treatments. The observed differences in resistance induction between MSNs-ss-SA and the other treatments could be explained as follows: (1) MSNs-ss-NH_2 grafted with SA via amide bonds could control the releases of SA under the action of rice-specific amidase, thereby extending its retention time in rice [78]; (2) the amidase and glutathione present in rice plants facilitated the degradation of MSNs-ss-SA to synchronize the release of SA and bioavailable silicon, which synergistically enhanced the disease resistance of plants [79].

Effects on rice resistance-related physical barriers

To achieve an optimal balance between cost-effectiveness and efficacy in managing sheath blight, a concentration of 1.0 mM MSNs-ss-SA was used in subsequent experiments to investigate its mechanism on enhancement of rice disease resistance. Rice plants at the booting stage were treated with SA, MSNs-ss-OH, MSNs-ss-OH and SA, or MSNs-ss-SA, followed by inoculation with the sheath blight pathogen (*R. solani*) three days after treatment.

Impacts on Callose deposition

To assess callose deposition, rice stem sections were stained with aniline blue and then observed under fluorescence microscopy 7 d after inoculation. As shown in Figs. 7A-E, all the treatments significantly increased the callose deposition values in the phloem. Compared to the water-treated control, callose deposition was increased by 1.07-fold in SA treated plants, 1.11-fold in MSNs-ss-OH treated plants, and 1.18-fold in MSNs-ss-OH and SA treated plants. Notably, MSNs-ss-SA treatment led to the highest enhancement, with callose deposition reaching approximately 1.3-fold greater than that of the control (Fig. 7F). These results indicated the effectiveness of both MSNs-ss-OH and SA in promoting callose deposition in rice stems. Therefore, the obtained nanosystem facilitated the simultaneous, controlled release of SA and bioavailable silicon, further enhancing callose deposition and reinforcing the defense of rice against plant pathogens [80, 81].

Effects on lignin content

Lignin, a critical component of the secondary cell wall, plays an essential role in reinforcing the mechanical integrity of the cell wall, thereby forming an effective physical barrier against pathogen invasion [82]. In this

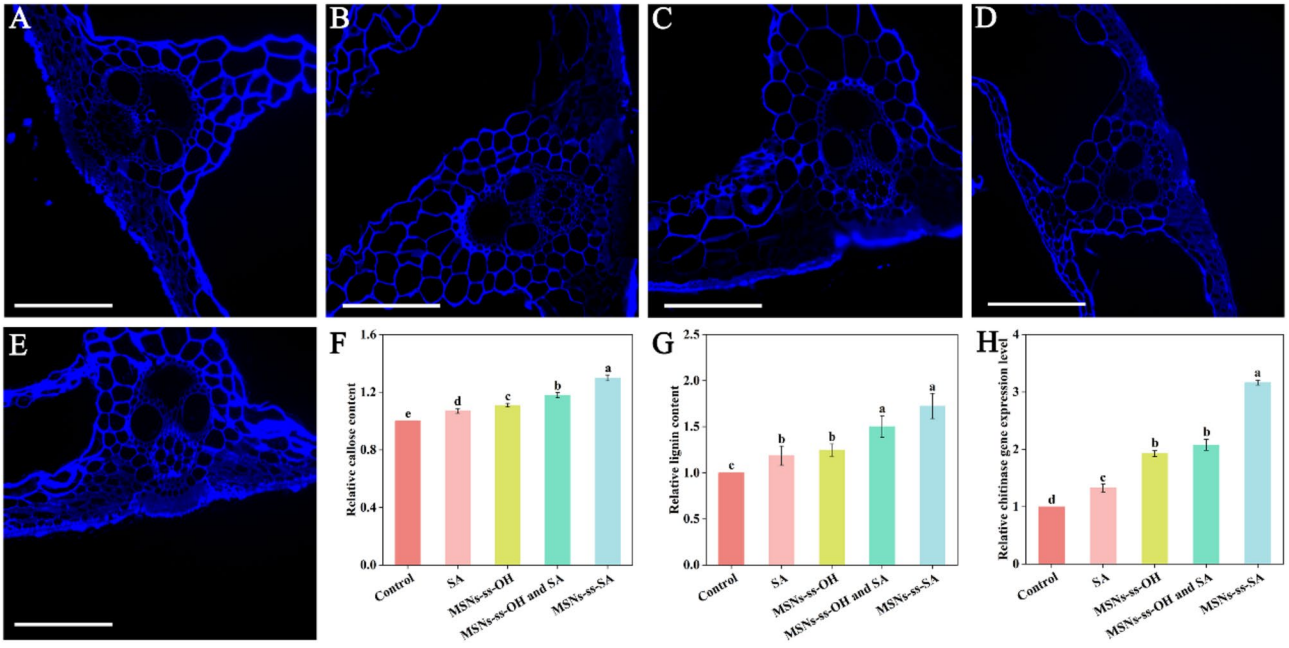

Fig. 7 Rice plants at the booting stage were treated with water (control) (**A**), SA (**B**), MSNs-ss-OH (**C**), MSNsss-OH and SA (**D**), or MSNs-ss-SA (**E**), followed by inoculation with the sheath blight pathogen (*R. solani*) three days after treatment. At seven days postinoculation, callose deposition patterns in rice stem tissues were analyzed. Rice stems were processed using paraffin embedding and sectioning, followed by staining with aniline blue dye (pH 8). Scale bar: 100 μm. Relative content of callose (**F**), relative content of lignin (**G**), and relative expression level of the chitinase gene (**H**) in rice stems. Error bars represent SD and different capital letters represent significant differences at $p < 0.05$ (Duncan test)

study, the lignin content in rice stems was measured using spectrometric analysis at 7 d after inoculation with *R. solani*. As shown in Fig. 7G, compared with the control treatment, SA, MSNs-ss-OH, MSNs-ss-OH and SA, and MSNs-ss-SA treatments significantly increased the lignin content. Specifically, lignin levels were increased by 1.19-fold in SA treated plants, 1.25-fold in MSNs-ss-OH treated plants, 1.50-fold in MSNs-ss-OH and SA treated plants, and 1.73-fold in MSNs-ss-SA treated plants, respectively. The MSNs-ss-SA treatment resulted in the highest lignin content increase (1.73-fold) among all treatments, likely due to the synergistic release of active components such as SA and bioavailable silicon, which substantially activated lignin biosynthesis pathways in rice plants [83, 84].

Chitinase gene expression

Chitinase plays a pivotal role in plant disease resistance by degrading fungal cell walls [85]. To investigate the molecular mechanism underlying the immune enhancement mediated by MSNs-ss-SA, the expression level of chitinase-related gene in rice stems was analyzed. As shown in Fig. 7H, all the treatments upregulated chitinase gene expression compared to the control, with MSNs-ss-SA inducing the most significant increase (> 3-fold). These results indicated that MSNs-ss-SA significantly enhanced the expression of chitinase-related gene through the synergistic release of SA and bioavailable silicon, thereby effectively degrading pathogen cell walls and reinforcing rice immunity [86].

Effects on hormone content

SA and JA are essential endogenous plant hormone signaling molecules that play pivotal roles in inducing plant defense responses and enhancing inherent resistance to plant diseases [87]. As illustrated in Fig. 8A and B, the SA, MSNs-ss-OH, and MSNs-ss-OH and SA treatments resulted in increases in the SA and JA contents, ranging from 27.90 to 59.65% and 48.14–116.11%, respectively. Notably, the MSNs-ss-SA treatment induced the most significant increase in both SA and JA contents, with a 99.06% increase in SA and a 213.85% increase in

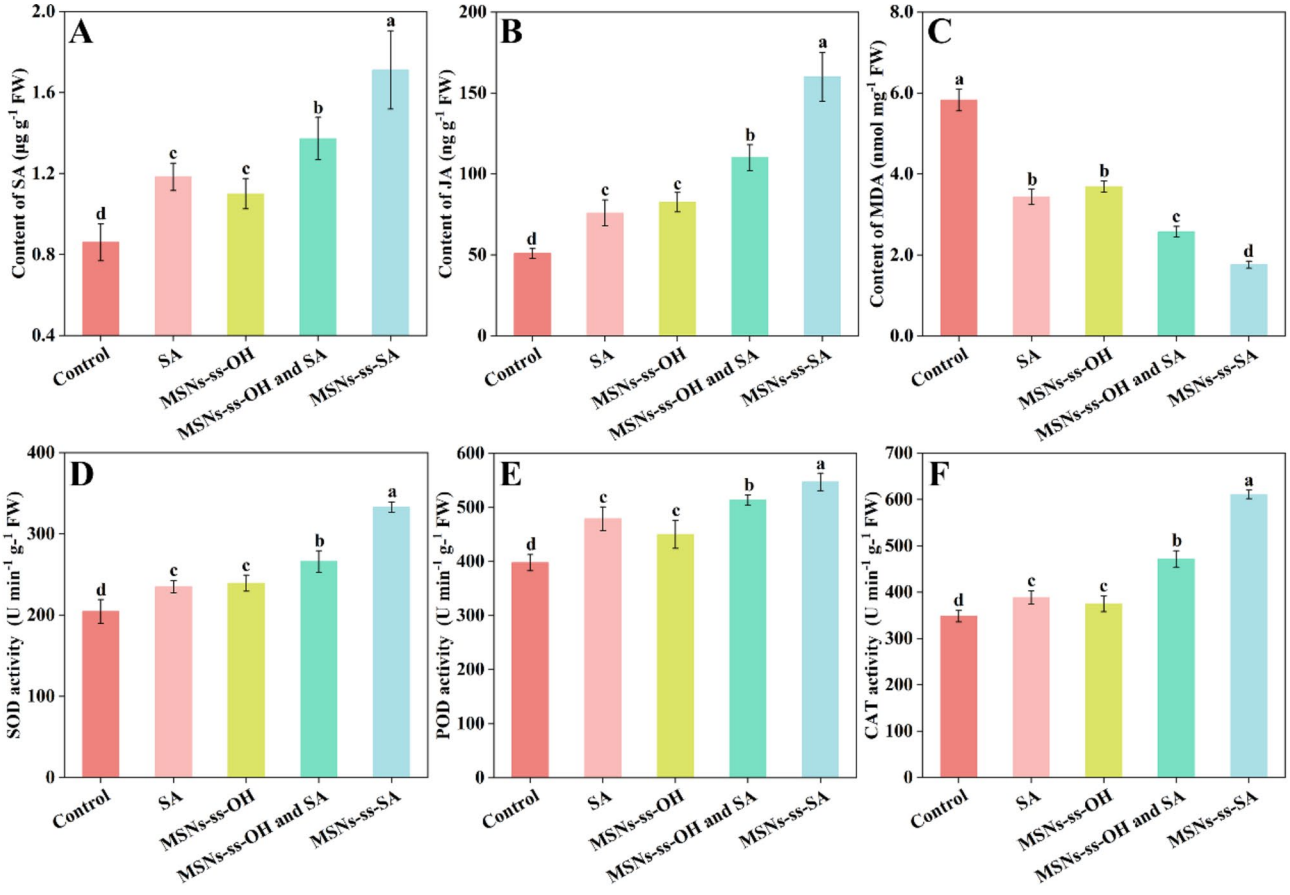

Fig. 8 Rice plants at the booting stage were treated with SA, MSNs-ss-OH, MSNs-ss-OH and SA, or MSNs-ss-SA, followed by inoculation with the sheath blight pathogen (*R. solani*) three days after treatment. Fourteen days post-inoculation, the endogenous SA content (**A**), JA content (**B**), MDA content (**C**), SOD activity (**D**), POD activity (**E**), and CAT activity (**F**) in rice stems were quantified. Error bars represent SD and different capital letters represent significant differences at $p < 0.05$(Duncan test)

JA compared with that of control group. The increase in both hormones was likely attributed to the controlled-release mechanism of the prodrug nanosystem.

Effects on the antioxidative system

To evaluate the effects of MSNs-ss-SA on the antioxidative defense system in rice, the key indicators of lipid peroxidation (such as the MDA content) and the activities of critical antioxidant enzymes (SOD, POD, and CAT) were quantified in rice stems [88]. As shown in Fig. 8C, all the treatments significantly reduced the MDA levels in the rice stems. Notably, the MSNs-ss-SA treatment had the most pronounced effect, with MDA levels decreasing by 70% with that in the control group, suggesting its effective alleviation of pathogen-induced damage to plant cells. Furthermore, MSNs-ss-SA demonstrated the most significant enhancement in antioxidative activity, with SOD, POD, and CAT activities increasing by 62.79%, 37.48%, and 75.42%, respectively, compared with that in the untreated control plants (Figs. 8D-F). The application of MSNs-ss-SA effectively mitigated the detrimental effects of pathogen infection on membrane lipid peroxidation and the antioxidative defense system in rice.

Regulation of disease resistance genes in rice

To investigate the regulatory effects of different treatments on rice disease resistance, this study quantitatively analyzed the expression levels of key genes in the SA and JA signaling pathways, which are closely related to plant immunity. The SA pathway plays a crucial role in SAR, while the JA pathway is primarily associated with ISR [89, 90]. Specifically, the expression levels of SA-related genes (*OsPR1a* and *OsWRKY45*) and JA-related genes (*OsAOS2* and *OsJAMYB*) were quantitatively analyzed under different treatment conditions. The results demonstrated that all the treatments significantly upregulated these defense-related genes, with the MSNs-ss-SA treatment resulting in the highest levels of gene expression. In the SA pathway, compared to the control group, the SA, MSNs-ss-OH, MSNs-ss-OH and SA, and MSNs-ss-SA treatments increased *OsPR1a* expression by 50%, 60%, 70%, and 100%, respectively (Fig. 9A). Similarly, *OsWRKY45* expression was upregulated by 50%, 75%, 100%, and 150% in the respective treatments (Fig. 9B). The pronounced upregulation of these SA-responsive genes suggested an enhanced SAR response in rice plants. In the JA pathway, all the treatments significantly increased the expression of *OsAOS2* and *OsJAMYB*, key genes involved in ISR activation. Compared with that in the control, *OsAOS2* expression increased by 100%, 200%, 300%, and 400% in the SA, MSNs-ss-OH, MSNs-ss-OH and SA, and MSNs-ss-SA treatment groups, respectively (Fig. 9C). Similarly, *OsJAMYB* expression was enhanced by 50%, 75%, 100%, and 150% across the different treatments (Fig. 9D). These findings indicated that JA-mediated defense responses were significantly strengthened, particularly under the MSNs-ss-SA treatment. Overall, this study confirmed that MSNs-ss-SA effectively modulated rice disease resistance by simultaneously activating the SA and JA pathways. The substantial upregulation of *OsPR1a* and *OsWRKY45* supported an enhanced SAR, while the increased expression of *OsAOS2* and *OsJAMYB* reinforced ISR. These findings indicate that MSNs-ss-SA induced strong activation of the SAR and ISR, significantly enhancing plant resistance to pathogens via a prodrug nanosystem-mediated dual hormone signaling mechanism.

Based on the above findings, the proposed mechanism by which MSNs-ss-SA enhances disease resistance in rice is illustrated in Fig. 1B. When MSNs-ss-SA (approximately 90 nm in size) are applied to rice leaves, they are rapidly absorbed through the stomata, resulting in efficient cellular entry and uniform tissue distribution. Within the plant, MSNs-ss-SA undergo gradual degradation mediated by endogenous amidase and glutathione, which cleave the amide and disulfide bonds in their framework. This degradation facilitates the controlled, simultaneous release of SA and bioavailable silicon. The released SA and silicon synergistically reinforce structural defense mechanisms by increasing callose and lignin deposition, activating the antioxidant defense system (SOD, POD, and CAT), and upregulating defense-related genes (*OsPR1a*, *OsWRKY45*, *OsAOS2*, and *OsJAMYB*). These molecular responses activate the SAR and ISR of rice plants, thereby significantly enhancing their resistance to pathogens.

Biosafety evaluation

To evaluate the environmental safety of MSNs-ss-SA, comprehensive assessments were conducted using *Oryza sativa*, *Daphnia magna*, *Eisenia fetida*, and human hepatocyte L02 cells as representative model organisms for plants, aquatic systems, soil ecosystems, and human health, respectively. As shown in Figs. 10A-D, no significant differences were observed in the chlorophyll content, shoot height, shoot fresh weight, or shoot dry weight of rice seedlings treated with various concentrations of MSNs-ss-SA compared with that in the water treatment (control). At an SA concentration of 8.0 mM within MSNs-ss-SA, no phytotoxic effect was observed, demonstrating its excellent safety for rice plants. In the case of *Daphnia magna* (Fig. 10E), a model organism for aquatic environments, both SA and MSNs-ss-SA exhibited dose-dependent toxicity. However, the LC_{50} value of MSNs-ss-SA was determined to be 1.98 mM, approximately six times greater than that of free SA (LC_{50} = 0.336 mM), indicating a significant reduction in toxicity due to the grafting of SA molecules onto MSNs-ss-NH_2.

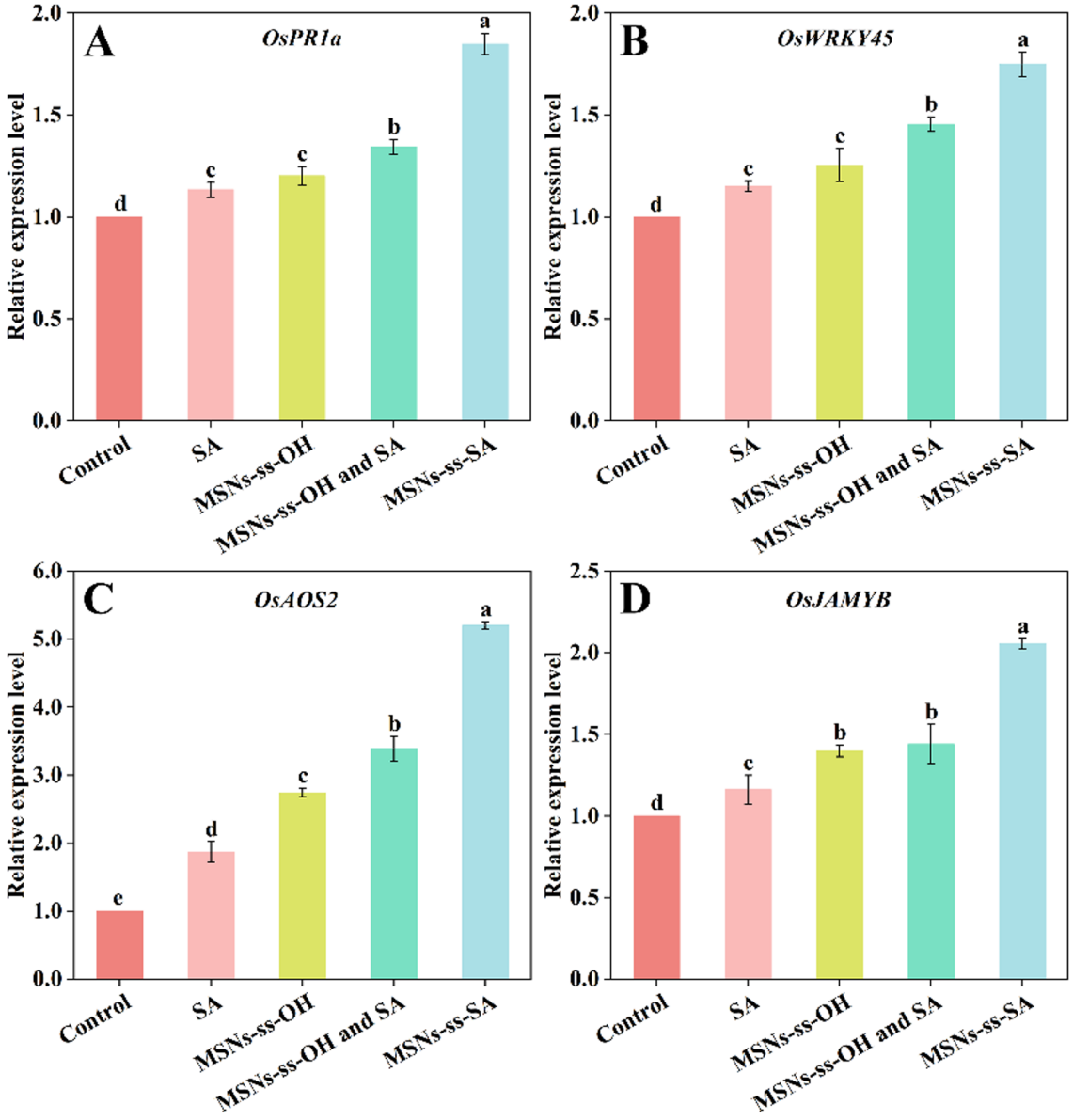

Fig. 9 Rice plants at the booting stage were treated with SA, MSNs-ss-OH, MSNs-ss-OH and SA, or MSNs-ss-SA, followed by inoculation with the sheath blight pathogen (*R. solani*) three days after treatment. Fourteen days post-inoculation, the relative gene expression levels of *OsPR1a* (**A**), *OsWRKY45* (**B**), *OsAOS2* (**C**), and *OsJAMYB* (**D**) in rice stems were measured. The gene expression levels were normalized using *eEF1a* (AB013606) as an internal control. Error bars represent SD and different capital letters represent significant differences at $p < 0.05$(Duncan test)

Similarly, in the soil model organism *Eisenia fetida* (Fig. 10F), MSNs-ss-SA (LC_{50} = 861.28 mg/kg) demonstrated significantly lower toxicity compared to free SA (LC_{50} = 166.38 mg/kg), which reduced their acute toxicity on non-target soil organisms by approximately five-fold. More importantly, the cytotoxicity of MSN-ss-SA and free SA was further evaluated in human hepatocyte L02 cells (Figs. 10G-I). At the same SA concentration, cell viability (Q4 represents viable cells) in the MSN-ss-SA treatment (92.8%) was slightly lower than the water control (93.4%) but higher than the SA treatment (92.1%). The total apoptosis rate (Q2 and Q3, represent late-stage apoptotic cells and early apoptotic cells) for MSN-ss-SA (6.23%) was marginally elevated compared to the water control (5.42%) but remained lower than free SA (7.12%). These results indicate that the prodrug nanosystem has excellent safety in plants, aquatic organisms, soil ecosystems, and human cell models, making it a promising candidate for sustainable disease management.

Effects on rice yield and quality

As shown in Table S5, as the concentration of MSNs-ss-SA increased, both rice varieties showed higher yields, with a significant increase observed at higher

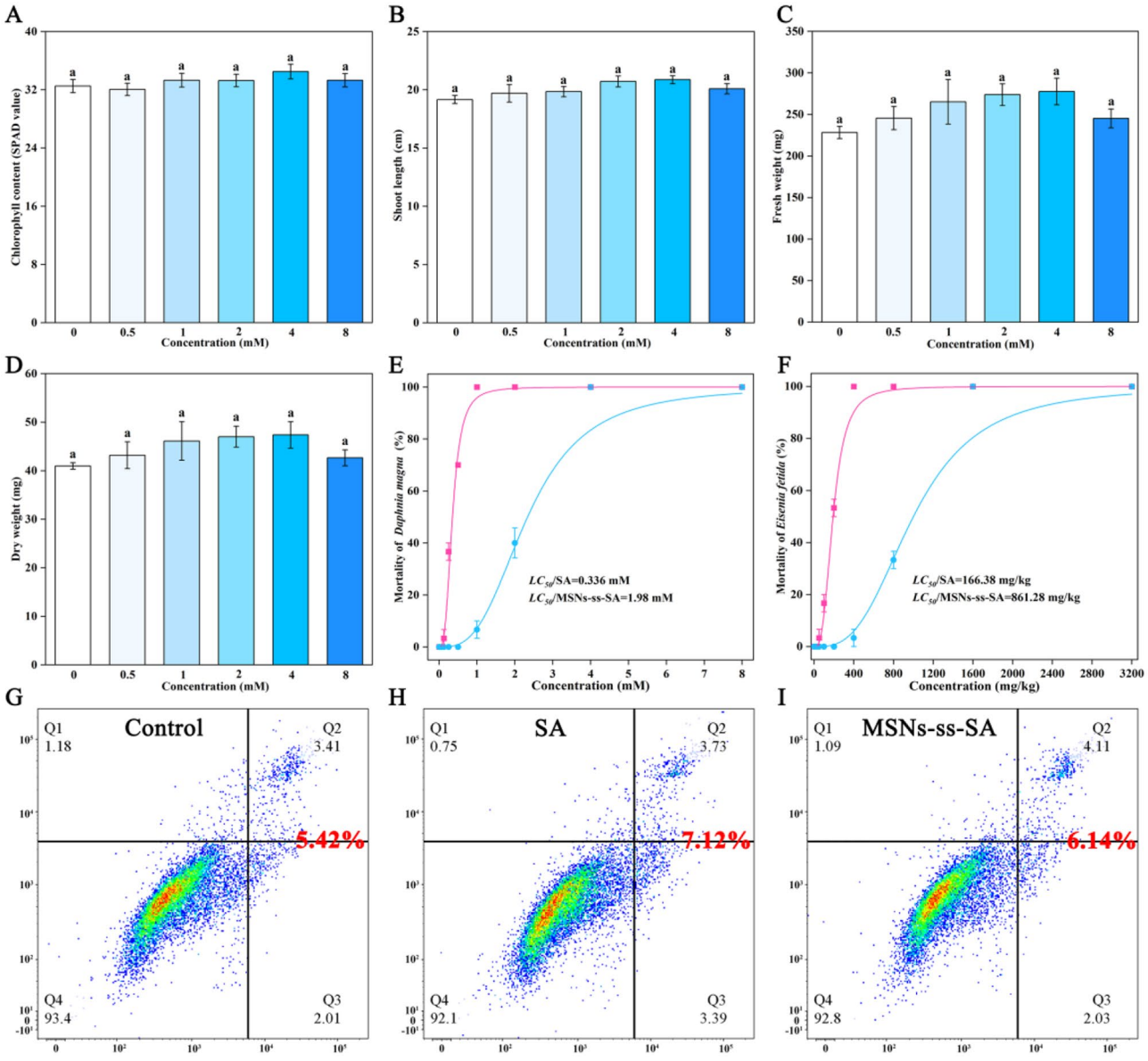

Fig. 10 Effects of foliar application of MSNs-ss-SA on the physiological and growth parameters of rice seedlings, including the leaf SPAD value (**A**), shoot height (**B**), shoot fresh weight (**C**), and shoot dry weight (**D**). Concentration-response curves for mortality occurrence (%) in *Daphnia magna* after 2 d of treatment with SA and MSNs-ss-SA (**E**), and in *Eisenia fetida* after 14 d of treatment with SA or MSNs-ss-SA (**F**). The ratio of apoptotic and necrotic cells in human hepatocyte L02 cells after treatment with control (**G**), SA (**H**), and MSNs-ss-SA (**I**). Error bars represent SD and different capital letters represent significant differences at $p < 0.05$(Duncan test)

concentrations (1.0 mM and 4.0 mM), ranging from 10.10 to 16.92%. This yield improvement was closely correlated with increases in the seed setting rate (1.98–5.34%) and 1,000-grain weight (1.13–1.66%). MSNs-ss-SA likely enhanced the stress tolerance of rice plants and improved the nutritional supply to the grains, thereby promoting grain filling and plumpness, in turn increasing the 1,000-grain weight and seed setting rate. However, owing to the pre-determined number of panicles per unit area and grains per panicle at the booting stage, MSNs-ss-SA showed a limited impact on these parameters.

Further investigation of the effect of MSNs-ss-SA on rice quality (Table S6) revealed an increase in the whole milled rice rate at higher concentrations, particularly at 1.0 mM and 4.0 mM, with a significant improvement of 5.98–8.63%. However, no significant changes were detected in the brown rice rate, milled rice rate, chalky grain rate, chalkiness degree, protein content, or amylose content at all concentrations. The observed yield improvement may correlate with enhanced stress tolerance and nutrient allocation, though further field trials are required to confirm these mechanisms. However, its

direct impact on intrinsic quality parameters, such as the brown rice rate, milled rice rate, chalky grain rate, chalkiness degree, protein content, and amylose content remain limited, as these traits are largely influenced by genetic factors, environmental conditions, and cultivation practices.

Conclusions

In this work, an amidase- and redox-responsive mesoporous silica-based prodrug (MSNs-ss-SA) was developed for the controlled and efficient delivery of SA and bioavailable silicon. The synthesized nanosystem was systematically characterized using TEM, element mapping, EDX spectroscopy, ^{13}C MAS NMR, XRD, zeta potential, FTIR, XPS, nitrogen adsorption-desorption, and TGA analysis. The nanosystem, with a size of approximately 90 nm, readily penetrated the stomata of rice leaves, where amidases and glutathione in the plant degraded the disulfide and amide bonds, triggering the sustained release of SA and bioavailable silicon within plant cells. By prolonging the duration of SA -induced disease resistance in plants, the nanosystem enhanced various plant defense mechanisms, including reinforcement of physical barriers (lignin and suberin deposition), upregulation of antioxidant defense enzymes (POD, SOD, and CAT), the activation of defense-related genes (*OsPR1a*, *OsWRKY45*, *OsAOS2*, and *OsJAMYB*), and the stimulation of chitinase synthesis. These actions collectively induced both SAR and ISR in rice, leading to long-term immune protection against plant diseases. Additionally, MSNs-ss-SA demonstrated excellent safety for both target and nontarget organisms, while also improving rice yield and processing quality. Therefore, the prodrug nanosystem provides an innovative and sustainable approach for modern agricultural disease management by enhancing crop resistance to pathogens and reducing reliance on chemical pesticides. Although this study highlights the potential of the MSNs-ss-SA nanosystem in enhancing disease resistance in rice, several limitations must be addressed to advance its translational application. First, the experiments were conducted using a single crop model (*Oryza sativa* L. cv. Lemont), and it is unclear whether the findings can be applied to other plant species or different rice varieties. Second, while the research focused on short-term effects under controlled greenhouse conditions, it lacks validation through field trials in different regions with varying environmental conditions (e.g., different soil types, temperatures, and rainfall). Such trials are necessary to evaluate the effectiveness and long-term environmental impact of the nanosystem. Finally, although the nanosystem controls diseases by boosting plant immunity, its slower action compared to conventional chemical fungicides limits its utility in rapid pathogen outbreak scenarios. Addressing these limitations will determine how effectively nanotechnology can be incorporated into sustainable pest management systems, ultimately balancing effectiveness, environmental safety, and economic feasibility.

Supplementary Information

The online version contains supplementary material available at https://doi.org/10.1186/s12951-025-03416-9.

Supplementary Material 1

Acknowledgements
We thank the staff of the Analysis and Testing Center of Yangzhou University for their technical assistance.

Author contributions
Y.L, Y.D. and Y.S. conceived and completed the experiments. S.W. designed and characterized the prodrug nanosystem. Y.D. and C.Z. cultured the rice seedlings, carried out the pathogenicity tests, and wrote the manuscript draft. Z.F. performed the data analysis. S.Z. provided ***R. solani*** (YN-7). F.P. provided theoretical guidance. K.X. and Z.H. assisted with the article draft modification. All the authors read and approved the final manuscript.

Funding
This work was supported by the National Natural Science Foundation of China (32102293), the National Key Laboratory of Green Pesticide, Guizhou University (GPLKF202506), the Carbon Peak Carbon Neutral Science and Technology Innovation Special Fund of Jiangsu Province (BE2022424), the Jiangsu Agricultural Science and Technology Innovation Fund (CX(24)2008 and CX(22)1001), the Earmarked Fund for CARS (Rice, CARS-01-26), the Postgraduate Research & Practice Innovation Program of Jiangsu Province (KYCX23_3578 and SJCX24_2276), the College Students' Innovative Entrepreneurial Training Plan Program (202411117194Y), and the Priority Academic Program Development of Jiangsu Higher Education Institutions (PAPD).

Data availability
No datasets were generated or analysed during the current study.

Declarations

Ethics approval and consent to participate
Not applicable.

Consent for publication
All the authors agree for publication.

Competing interests
The authors declare no competing interests.

Author details
[1]Co-Innovation Center for Modern Production Technology of Grain Crop, Jiangsu Key Laboratory of Crop Genetics and Physiology, Research Institute of Rice Industrial Engineering Technology, Yangzhou University, Yangzhou 225009, China
[2]State Key Laboratory of Green Pesticide, Key Laboratory of Green Pesticide and Agricultural Bioengineering, Ministry of Education, Center for Research and Development of Fine Chemicals, Guizhou University, Guiyang 550025, China
[3]College of Bioscience and Biotechnology, Yangzhou University, Yangzhou 225009, China

Received: 19 February 2025 / Accepted: 23 April 2025
Published online: 07 May 2025

References

1. Ristaino JB, Anderson PK, Bebber DP, Brauman KA, Cunniffe NJ, Fedoroff NV, Finegold C, Garrett KA, Gilligan CA, Jones CM, Martin MD, MacDonald GK, Neenan P, Records A, Schmale DG, Tateosian L, Wei Q. The persistent threat of emerging plant disease pandemics to global food security. Proc Natl Acad Sci USA., 2021;118:e2022239118.
2. Singh BK, Delgado-Baquerizo M, Egidi E, Guirado E, Leach JE, Liu H, Trivedi P. Climate change impacts on plant pathogens, food security and paths forward. Nat Rev Microbiol. 2023;21:640–56.
3. Zhou W, Li M, Achal V. A comprehensive review on environmental and human health impacts of chemical pesticide usage. Emerg Contam. 2025;11:100410.
4. Ritchie H, Roser M, Rosado P. Pesticides, Published online at OurWorldInData.org;2022. Retrieved from https://ourworldindata.org/pesticides
5. Singh A, Shraogi N, Verma R, Saji J, Kumar Kar A, Tehlan S, Ghosh D, Patnaik S. Challenges in current pest management practices: navigating problems and a way forward by integrating controlled release system approach. Chem Eng J. 2024;498:154989.
6. Pimentão AR, Cuco AP, Pascoal C, Cássio F, Castro BB. Current trends and mismatches on fungicide use and assessment of the ecological effects in freshwater ecosystems. Environ Pollut. 2024;347:123678.
7. Meena M, Yadav G, Sonigra P, Nagda A, Mehta T, Swapnil P, Harish A, Marwal. Role of elicitors to initiate the induction of systemic resistance in plants to biotic stress. Plant Stress. 2022;5:100103.
8. Zhu F, Cao M-Y, Zhang Q-P, Mohan R, Schar J, Mitchell M, Chen H, Liu F, Wang D, Fu ZQ. Join the green team: inducers of plant immunity in the plant disease sustainable control toolbox. J Adv Res. 2024;57:15–42.
9. De Vleesschauwer D, Chernin L, Höfte MM. Differential effectiveness of *Serratia plymuthica* IC1270-induced systemic resistance against hemibiotrophic and necrotrophic leaf pathogens in rice. BMC Plant Biol. 2009;9:9.
10. Chalupowicz L, Manulis-Sasson S, Barash I, Elad Y, Rav-David D, Brandl MT. Effect of plant systemic resistance elicited by biological and chemical inducers on the colonization of the lettuce and basil leaf apoplast by *Salmonella enterica*. Environ Microbiol. 2021;87:e01151–21.
11. Shafqat A, Abbas S, Ambreen M, Siddiqa Bhatti A, kausar H, Gull T. Exploring the vital role of phytohormones and plant growth regulators in orchestrating plant immunity. Physiol Mol Plant Pathol. 2024;133:102359.
12. Roychowdhury R, Mishra S, Anand G, Dalal D, Gupta R, Kumar A, Gupta R. Decoding the molecular mechanism underlying salicylic acid (SA)-mediated plant immunity: an integrated overview from its biosynthesis to the mode of action. Physiol Plant. 2024;176:e14399.
13. Noutoshi Y, Ito T, Seki M, Nakashita H, Yoshida S, Marco Y, Shirasu K, Shinozaki K. A single amino acid insertion in the WRKY domain of the *Arabidopsis* TIR–NBS–LRR–WRKY-type disease resistance protein SLH1 (sensitive to low humidity 1) causes activation of defense responses and hypersensitive cell death. Plant J. 2005;43:873–88.
14. Yan Y, Pan C, Du Y, Li D, Liu W. Exogenous salicylic acid regulates reactive oxygen species metabolism and ascorbate–glutathione cycle in *Nitraria tangutorum* Bobr. under salinity stress. Physiol Mol Biol Plants. 2018;24:577–89.
15. Pasternak T, Groot EP, Kazantsev FV, Teale W, Omelyanchuk N, Kovrizhnykh V, Palme K, Mironova VV. Salicylic acid affects root meristem patterning via auxin distribution in a concentration-dependent manner. Plant Physiol. 2019;180:1725–39.
16. Yi Z, Hussain HI, Feng C, Sun D, She F, Rookes JE, Cahill DM, Kong L. Functionalized mesoporous silica nanoparticles with redox-responsive short-chain gatekeepers for agrochemical delivery. ACS Appl Mater Interfaces. 2015;7:9937–46.
17. Huang X, Zhu G, Liu Q, Chen L, Li Y, Hou B. Modulation of plant salicylic acid-associated immune responses via glycosylation of dihydroxybenzoic acids. Plant Physiol. 2018;176:3103–19.
18. Feng C, Tian X, Wang X, Cui M, Xu C, Wang W, Wang W. Fabrication of salicylic acid nanosphere for long-term induced immunity performance. RSC Adv. 2020;10:28576–84.
19. Huang Y, Wang H, Tang G, Zhou Z, Zhang X, Liu Y, Yan G, Wang J, Hu G, Xiao J, Yan W, Cao Y. Fabrication of pH-responsive nanoparticles for co-delivery of fungicide and salicylic acid with synergistic antifungal activity. J Clean Prod. 2024;451:142093.
20. Saitoh Y, Mitani-Ueno N, Saito K, Matsuki K, Huang S, Yang L, Yamaji N, Ishikita H, Shen J-R, Ma JF, Suga M. Structural basis for high selectivity of a rice silicon channel Lsi1, Nat. Commun. 2021;12:6236.
21. Mahawar L, Ramasamy KP, Suhel M, Prasad SM, Živčák M, Brestic M, Rastogi A, Skalický M. Silicon nanoparticles: Comprehensive review on biogenic synthesis and applications in agriculture. Environ Res. 2023;232:116292.
22. Mathur P, Roy S. Nanosilica facilitates silica uptake, growth and stress tolerance in plants. Plant Physiol Biochem. 2020;157:114–27.
23. Bhat JA, Rajora N, Raturi G, Sharma S, Dhiman P, Sanand S, Shivaraj SM, Sonah H, Deshmukh R. Silicon nanoparticles (SiNPs) in sustainable agriculture: Major emphasis on the practicality, efficacy and concerns. Nanoscale Adv. 2021;3:4019–28.
24. Wang J, Cao X, Wang C, Xiao Z, Chen F, Feng Y, Yue L, Wang Z, Xing B. Transcriptomics and metabolomics reveal the mechanisms of enhanced constitutive resistance in rice (*Oryza sativa* L.) by silica nanomaterials. Environ Sci: Nano. 2023;10:2831–48.
25. Yuvaraj M, Sathya Priya R, Jagathjothi N, Saranya M, Suganthi N, Sharmila R, Cyriac J, Anitha R, Subramanian KS. Silicon nanoparticles (SiNPs): Challenges and perspectives for sustainable agriculture. Physiol Mol Plant Pathol. 2023;128:102161.
26. Sathe AP, Kumar A, Mandlik R, Raturi G, Yadav H, Kumar N, Shivaraj SM, Jaswal R, Kapoor R, Gupta SK, Sharma TR, Sonah H. Role of silicon in elevating resistance against sheath blight and blast diseases in rice (*Oryza sativa* L). Plant Physiol Biochem. 2021;166:128–39.
27. Khan I, Awan SA, Rizwan M, brestic M, Xie W. Silicon: an essential element for plant nutrition and phytohormones signaling mechanism under stressful conditions. Plant Growth Regul. 2023;100:301–19.
28. Joshi H. Exploring the efficacy of green nanoparticles in enhancing plant defense: a mechanistic investigation into immune response activation. J Nanopart Res. 2025;27:29.
29. El-Shetehy M, Moradi A, Maceroni M, Reinhardt D, Petri-Fink A, Rothen-Rutishauser B, Mauch F, Schwab F. Silica nanoparticles enhance disease resistance in *Arabidopsis* plants. Nat Nanotechnol. 2021;16:344–53.
30. Du J, Liu B, Zhao T, Xu X, Lin H, Ji Y, Li Y, Li Z, Lu C, Li P, Zhao H, Li Y, Yin Z, Ding X. Silica nanoparticles protect rice against biotic and abiotic stresses. J Nanobiotechnol. 2022;20:197.
31. Ehrlich H, Demadis KD, Pokrovsky OS, Koutsoukos PG. Modern views on desilicification: Biosilica and abiotic silica dissolution in natural and artificial environments. Chem Rev. 2010;110:4656–89.
32. Croissant JG, Fatieiev Y, Khashab NM. Degradability and clearance of silicon, organosilica, silsesquioxane, silica mixed oxide, and mesoporous silica nanoparticles. Adv Mater. 2017;29:1604634.
33. Liang Y, Gao Y, Wang W, Dong H, Tang R, Yang J, Niu J, Zhou Z, Jiang N, Cao Y. Fabrication of smart stimuli-responsive mesoporous organosilica nanovehicles for targeted pesticide delivery. J Hazard Mater. 2020;389:122075.
34. Qi Q, Shen Q, Geng J, An W, Wu Q, Wang N, Zhang Y, Li X, Wang W, Yu C, Li L. Stimuli-responsive biodegradable silica nanoparticles: from native structure designs to biological applications. Adv Colloid Interface Sci. 2024;324:103087.
35. Jiang C, Shimono M, Sugano S, Kojima M, Liu X, Inoue H, Sakakibara H, Takatsuji H. Cytokinins act synergistically with salicylic acid to activate defense gene expression in rice. Mol Plant-Microbe Interact. 2013;26:287–96.
36. Kouzai Y, Kimura M, Watanabe M, Kusunoki K, Osaka D, Suzuki T, Matsui H, Yamamoto M, Ichinose Y, Toyoda K, Matsuura T, Mori IC, Hirayama T, Minami E, Nishizawa Y, Inoue K, Onda Y, Mochida K, Noutoshi Y. Salicylic acid-dependent immunity contributes to resistance against *Rhizoctonia solani*, a necrotrophic fungal agent of sheath blight, in rice and *Brachypodium distachyon*. New Phytol. 2018;217:771–83.
37. Saberi Riseh R, Vatankhah M, Hassanisaadi M, Kennedy JF. Chitosan/silica: A hybrid formulation to mitigate phytopathogens. Int J Biol Macromol. 2023;239:124192.
38. Shi H, Naqvi NI, Kou Y. Recent advances in targeted fungicides and immune elicitors for rice blast management. Plant Commun. 2024;5:101032.
39. Ding C, Zhang Y, Chen C, Wang J, Qin M, Gu Y, Zhang S, Wang L, Luo Y. Hollow mesoporous silica nanoparticles as a new nanoscale resistance inducer for Fusarium wilt control: Size effects and mechanism of action. Int J Mol Sci. 2024;25:4514.
40. Hacham Y, Koussevitzky S, Kirma M, Amir R. Glutathione application affects the transcript profile of genes in *Arabidopsis* seedling. J Plant Physiol. 2014;171:1444–51.
41. Jeong EM, Yoon J-H, Lim J, Shin J-W, Cho AY, Heo J, Lee KB, Lee J-H, Lee WJ, Kim H-J, Son YH, Lee S-J, Cho S-Y, Shin D-M, Choi K, Kim I-G. Real-time monitoring of glutathione in living cells reveals that high glutathione levels are required to maintain stem cell function. Stem Cell Rep. 2018;10:600–14.
42. Aziz M, Chapman KD. Fatty acid amide hydrolases: an expanded capacity for chemical communication? Trends Plant Sci. 2020;25:236–49.

43. Zhang L, Yao G, Mao Z, Song M, Zhao R, Zhang X, Chen C, Zhang H, Liu Y, Wang G, Li F, Wu X. Experimental and computational approaches to characterize a novel amidase that initiates the biodegradation of the herbicide propanil in *Bosea* Sp. P5. J Hazard Mater. 2023;451:131155.
44. Zhou X, Huang J, Xu S, Cheng H, Liu B, Huang J, Liu J, Pan D, Wu X. Novel bifunctional amidase catalyzing the degradation of propanil and aryloxyphenoxypropionate herbicides in *Rhodococcus* Sp. C-1. J Agric Food Chem. 2024;72:18067–77.
45. Hubálek F, Cramer CN, Helleberg H, Johansson E, Nishimura E, Schluckebier G, Steensgaard DB, Sturis J, Kjeldsen TB. Enhanced disulphide bond stability contributes to the once-weekly profile of insulin icodec. Nat Commun. 2024;15:6124.
46. Rotilio L, Bayer T, Meinert H, Teixeira LM, Johansen MB, Sommerfeldt A, Petersen AR, Sandahl A, Keller MB, Holck J. Structural and functional characterization of an amidase targeting a polyurethane for sustainable recycling. Angew Chem Int Ed. 2025;64:e202419535.
47. Sohail M, Pirzada T, Guenther R, Barbieri E, Sit T, Menegatti S, Crook N, Opperman CH, Khan SA. Cellulose acetate-stabilized Pickering emulsions: preparation, rheology, and incorporation of agricultural active ingredients. ACS Sustain Chem Eng. 2023;11:15178–91.
48. Liang Y, Jiang F, Xu D, Fu L, Xu C, Huang G, Lin B. Construction of a novel mathematical model for predicting pesticide release in soil and its application in rice pest control. J Clean Prod. 2024;436:140646.
49. Avellan A, Yun J, Morais BP, Clement ET, Rodrigues SM, Lowry GV. Critical review: role of inorganic nanoparticle properties on their foliar uptake and in planta translocation. Environ Sci Tech. 2021;55:13417–31.
50. Piršelová B, Mistríková V, Libantová J, Moravčíková J, Matušíková I. Study on metal-triggered Callose deposition in roots of maize and soybean. Biologia. 2012;67:698–705.
51. Chang XF, Chandra R, Berleth T, Beatson RP. Rapid, microscale, acetyl bromide-based method for high-throughput determination of lignin content in *Arabidopsis thaliana*. J Agric Food Chem. 2008;56:6825–34.
52. Martinez DST, Ellis L-JA, Da Silva GH, Petry R, Medeiros AMZ, Davoudi HH, Papadiamantis AG, Fazzio A, Afantitis A, Melagraki G, Lynch I. *Daphnia magna* and mixture toxicity with nanomaterials – Current status and perspectives in data-driven risk prediction. Nano Today. 2022;43:101430.
53. Ellis L-JA, Valsami-Jones E, Lynch I. Exposure medium and particle ageing moderate the toxicological effects of nanomaterials to *Daphnia magn*a over multiple generations: a case for standard test review? Environ Sci: Nano. 2020;7:1136–49.
54. Lisbôa RdM, Storck TR, Silveira AdO, Wolff D, Tiecher TL, Brunetto G, Clasen B. Ecotoxicological responses of *Eisenia andrei* exposed in field-contaminated soils by sanitary sewage. Ecotoxicol Environ Saf. 2021;214:112049.
55. Yuan Y, Teng H, Zhang T, Wang D, Gu H, Lv W. Toxicological effects induced by two carbamates on earthworms (*Eisenia fetida*): acute toxicity, arrested regeneration and underlying mechanisms. Ecotoxicol Environ Saf. 2024;269:115824.
56. Li C, You Y, Chen D, Gu Z, Zhang Y, Holler TP, Ban X, Hong Y, Cheng L, Li Z. A systematic review of rice noodles: Raw material, processing method and quality improvement. Trends Food Sci Technol. 2021;107:389–400.
57. Nithya A, Vishwakarma S, Dalbhagat CG, Mishra HN. Apparent amylose content positively influences the quality of extruded fortified rice kernels. Carbohydr Polym. 2024;338:122213.
58. Zhang J, Cheng Y, Tang N. Rapid analysis of protein content in rice noodles using NIR and FTIR spectroscopy for quality control of river snail rice noodle products. Food Control. 2025;168:110906.
59. Wagner J, Gößl D, Ustyanovska N, Xiong M, Hauser D, Zhuzhgova O, Hočevar S, Taskoparan B, Poller L, Datz S, Engelke H, Daali Y, Bein T, Bourquin C. Mesoporous silica nanoparticles as pH-responsive carrier for the immune-activating drug resiquimod enhance the local immune response in mice. ACS Nano. 2021;15:4450–66.
60. Cauda V, Engelke H, Sauer A, Arcizet D, Bräuchle C, Rädler J, Bein T. Colchicine-loaded lipid bilayer-coated 50 mesoporous nanoparticles efficiently induce microtubule depolymerization upon cell uptake. Nano Lett. 2010;10:2484–92.
61. Yan Y, Fu J, Wang T, Lu X. Controlled release of silyl ether camptothecin from thiol-ene click chemistry-functionalized mesoporous silica nanoparticles. Acta Biomater. 2017;51:471–8.
62. Hanrahan MP, Venkatesh A, Carnahan SL, Calahan JL, Lubach JW, Munson EJ, Rossini AJ. Enhancing the resolution of ^{1}H and ^{13}C solid-state NMR spectra by reduction of anisotropic bulk magnetic susceptibility broadening. Phys Chem Chem Phys. 2017;19:28153–62.
63. Maddalena R, Hall C, Hamilton A. Effect of silica particle size on the formation of calcium silicate hydrate [C-S-H] using thermal analysis. Thermochim Acta. 2019;672:142–9.
64. Falk G, Shinhe GP, Teixeira LB, Moraes EG, de Oliveira APN. Synthesis of silica nanoparticles from sugarcane bagasse ash and nano-silicon via magnesiothermic reactions. Ceram Int. 2019;45:21618–24.
65. Yan H, Hao L, Chen H, Zhou X, Ji H, Zhou H. Salicylic acid functionalized zein for improving plant stress resistance and as a nanopesticide carrier with enhanced anti-photolysis ability. J Nanobiotechnol. 2023;21:23.
66. Garrido M, Naranjo A, Pérez EM. Characterization of emerging 2D materials after chemical functionalization. Chem Sci. 2024;15:3428–45.
67. Ahlawat M, Sahu A, Govind Rao V. Harnessing Pb–S interactions for long-term water stability in cesium lead halide perovskite nanocrystals. Small. 2024;20:2401326.
68. Niu Y, Chen Y, Bao S, Sun H, Wang Y, Ge B, Li P, Hou Y. Fabrication of polyarylate thin-film nanocomposite membrane based on graphene quantum dots interlayer for enhanced gas separation performance. Sep Purif Technol. 2022;293:121035.
69. Huang Y-Y, Lee Z-H, Chang K-C, Wu Z-Y, Lee C-C, Tsou M-H, Lin H-M. Mesoporous silica nanoparticles with dual-targeting agricultural sources for enhanced cancer treatment via tritherapy. RSC Adv. 2023;13:19079–90.
70. Wang H, Qian C, Sun L, Jiang H, Wang X, Cui J, Yang D. A novel type of quantum-delivery system (salicylic acid conjugation based on ZnO quantum dots) alleviates the bacterial fruit blotch disease of melon plants by activating defense response. Chem Eng J. 2024;500:156901.
71. Alam M, Ahmed M, Altaf M, Shaik JP. Fabrication of multiwalled carbon nanotube-reinforced rapeseed-oil-based polyurethane coatings for anticorrosive applications. Polym Int. 2023;72:126–37.
72. Du X, Kleitz F, Li X, Huang H, Zhang X, Qiao S-Z. Disulfide-bridged Organosilica frameworks: designed, synthesis, redox-triggered biodegradation, and nanobiomedical applications. Adv Funct Mater. 2018;28:1707325.
73. Li W-Y, Wan J-J, Kan J-L, Wang B, Song T, Guan Q, Zhou L-L, Li Y-A, Dong Y-B. A biodegradable covalent organic framework for synergistic tumor therapy. Chem Sci. 2023;14:1453–60.
74. Phala K, Mapossa AB, Augustyn W, Combrinck S, Botha B. Development of EVA and LLDPE polymer-based carvone and spearmint essential oil release systems for citrus postharvest diseases applications. Arab J Chem. 2023;16:104458.
75. Long S, Yu M-J, Feng R, Tao H, Zhang B. Novel self-assembled micelles of dual-modified dextrin with pH responsiveness via grafted octenyl succinic anhydride and cysteamine for curcumin delivery. Food Chem. 2024;460:140748.
76. Hu P, An J, Faulkner MM, Wu H, Li Z, Tian X, Giraldo JP. Nanoparticle charge and size control foliar delivery efficiency to plant cells and organelles. ACS Nano. 2020;14:7970–86.
77. Yin J, Zhao J, Wang Z, Xue F, Wang Q, Guo H, Cheng H, Li J, Shen J, Yin M, Su X, Yan S. Preparation of salicylic acid nano-protectant with dual synergistic mechanism: high direct fungicidal activity and plant defence toward cotton Verticillium wilt. Chem Eng J. 2024;496:154036.
78. Dong Y, Jiang T, Wu T, Wang W, Xie Z, Yu X, Peng Y, Wang L, Xiao Y, Zhong T. Enzyme-responsive controlled-release materials for food preservation and crop protection - A review. Int J Biol Macromol. 2024;254:128051.
79. Shivappa R, B J, Ms B, Sr P, U K, M A, Pati P, Mohapatra SD, Govindharaj G-P-P. Dual role of potassium silicate and salicylic acid: Plant growth promotor and plant immunity booster against bakanae disease of rice. Silicon. 2024;16:1173–82.
80. Shanmugaiah V, Gauba A, Hari SK, Prasad R, Ramamoorthy V, Sharma MP. Effect of silicon micronutrient on plant's cellular signaling cascades in stimulating plant growth by mitigating the environmental stressors. Plant Growth Regul. 2023;100:391–408.
81. German L., Yeshvekar R, Benitez-Alfonso Y. Callose metabolism and the regulation of cell walls and plasmodesmata during plant mutualistic and pathogenic interactions. Plant Cell Environ. 2023;46:391–404.
82. Dora S, Terrett OM, Sánchez-Rodríguez C. Plant–microbe interactions in the apoplast: communication at the plant cell wall. Plant Cell. 2022;34:1532–50.
83. Pan J, Guan M, Xu P, Chen M, Cao Z. Salicylic acid reduces cadmium (Cd) accumulation in rice (*Oryza sativa* L.) by regulating root cell wall composition via nitric oxide signaling. Sci Total Environ. 2021;797:149202.
84. Xiao Z, Fan N, Zhu W, Qian H-L, Yan X-P, Wang Z, Rasmann S. Silicon nanodots increase plant resistance against herbivores by simultaneously activating physical and chemical defenses. ACS Nano. 2023;17:3107–18.
85. Martínez-Cruz J, Romero D, Hierrezuelo J, Thon M, de Vicente A, Pérez-García A. Effectors with chitinase activity (EWCAs), a family of conserved, secreted

fungal chitinases that suppress chitin-triggered immunity. Plant Cell. 2021;33:1319–40.
86. Jeong G-J, Khan F, Tabassum N, Kim Y-M. Chitinases as key virulence factors in microbial pathogens: Understanding their role and potential as therapeutic targets. Int J Biol Macromol. 2023;249:126021.
87. Li Z, Ahammed GJ. Salicylic acid and jasmonic acid in elevated CO_2-induced plant defense response to pathogens. J Plant Physiol. 2023;286:154019.
88. Ahmed T, Noman M, Jiang H, Shahid M, Ma C, Wu Z, Nazir MM, Ali MA, White JC, Chen J, Li B. Bioengineered chitosan-iron nanocomposite controls bacterial leaf blight disease by modulating plant defense response and nutritional status of rice (*Oryza sativa* L). Nano Today. 2022;45:101547.
89. Du D, Zhang C, Xing Y, Lu X, Cai L, Yun H, Zhang Q, Zhang Y, Chen X, Liu M, Sang X, Ling Y, Yang Z, Li Y, Lefebvre B, He G. The CC-NB-LRR OsRLR1 mediates rice disease resistance through interaction with OsWRKY19. Plant Biotechnol J. 2021;19:1052 -64.
90. Ye S, Zhou S, Ma Y, Yang J, Shi X, Zhang R, Yang Z, Peng D, Ding Z. Biocontrol activity and potential mechanism of *Bacillus cereus* G5 against *Meloidogyne graminicola*. Pestic Biochem Physiol. 2024;204:106079.

Publisher's note